Geophysical Journal International

Geophys. J. Int. (2010) doi: 10.1111/j.1365-246X.2010.04754.x

Extension on the Tibetan plateau: recent normal faulting measured by InSAR and body wave seismology

J. R. Elliott,[1] R. J. Walters,[1] P. C. England,[1] J. A. Jackson,[2] Z. Li[3] and B. Parsons[1]

[1] *COMET+, Department of Earth Sciences, University of Oxford, Parks Road, Oxford* OX1 3PR, *UK. E-mail: john.elliott@earth.ox.ac.uk*
[2] *COMET+, Department of Earth Sciences, University of Cambridge, Bullard Laboratories, Madingley Road, Cambridge,* CB3 0EZ, *UK*
[3] *COMET+, Department of Geographical and Earth Sciences, University of Glasgow, Glasgow,* G12 8QQ, *UK*

Accepted 2010 July 27. Received 2010 July 27; in original form 2009 September 25

SUMMARY

We use InSAR and body wave modelling to determine the faulting parameters for a series of five M_w 5.9–7.1 normal faulting earthquakes that occurred during 2008, including the March 20 Yutian earthquake (M_w 7.1), one of the largest normal faulting events to have occurred recently on the continents. We also study three earlier normal faulting earthquakes that occurred in southern Tibet between 1992 and 2005. Coseismic deformation for each of these eight events is measured with ascending and descending interferograms from ENVISAT, ERS and ALOS SAR data. Elastic dislocation modelling of the line-of-sight InSAR displacements and body wave seismological modelling of *P* and *SH* waves are used to estimate fault parameters and are found to be in good agreement for all the events studied. The use of InSAR to measure deformation allows a relatively precise determination of the fault location in addition to resolving the focal plane ambiguity. Only five of the eight events are associated with a clear surface topographic feature, suggesting that an underestimation of the amount of extension would result from using the surface expressions of normal faulting alone. The observations, in all cases, are consistent with slip on planar surfaces, with dips in the range 40–50°, that penetrates the uppermost crust to a depth of 10–15 km. We find no evidence for active low-angle (dip less than 30°) normal faulting. The contribution of the normal faulting to overall extension estimated by summing seismic moments over earthquakes for the past 43 yr is 3–4 mm yr^{-1}, or 15–20 per cent of the rates of extension measured across the plateau using GPS. 85 per cent of the moment release in normal faulting over the past 43 yr has occurred in regions whose surface height exceeds 5 km. This observation adds weight to the suggestions that the widespread normal faulting on the plateau is the result of variations in the gravitational potential energy of the lithosphere.

Key words: Satellite geodesy; Radar interferometry; Seismicity and tectonics; Body waves; Continental tectonics: extensional; Asia.

1 INTRODUCTION

Whilst much of the great elevation of the Tibetan plateau results from crustal thickening, the active tectonics of the high plateau are now characterized by a mixture of strike-slip and normal faulting accommodating convergence and extension. Active north–south trending grabens (Armijo *et al.* 1986), strike-slip faulting (Armijo *et al.* 1989), focal mechanisms (Molnar & Lyon-Caen 1989) and recent GPS measurements (Zhang *et al.* 2004) indicate that southern Tibet is extending in an approximately east–west direction, but few estimates currently exist for the contribution of normal faulting to this extension.

From GPS observations across the plateau, Zhang *et al.* (2004) estimate ENE–WSW stretching of 21.6 ± 2.5 mm yr^{-1} between 79°E and 93°E across the central plateau, with 10–14 mm yr^{-1} NNE–SSW shortening occurring between north of the Himalaya and south of the Altyn Tagh and Kunlun Faults; shortening to the south of Southern Tibet in the Himalaya is presumed to be caused by locking on the main frontal thrust (Cattin & Avouac 2000). As there are no active thrusts on the plateau (e.g. Armijo *et al.* 1986, 1989), convergence within Tibet must be accommodated by the strike-slip faulting, which also contributes to the east-west extension. Large, $M \sim 8$, earthquakes have occurred on strike-slip faults in Tibet (e.g. Armijo *et al.* 1989; Lasserre *et al.* 2005) and dominate the recent moment release there, but a series of M_w 5.9–7.1 normal faulting earthquakes in 2008 leads us to re-examine the contribution of normal faulting to the extension of the plateau.

© 2010 The Authors
Geophysical Journal International © 2010 RAS

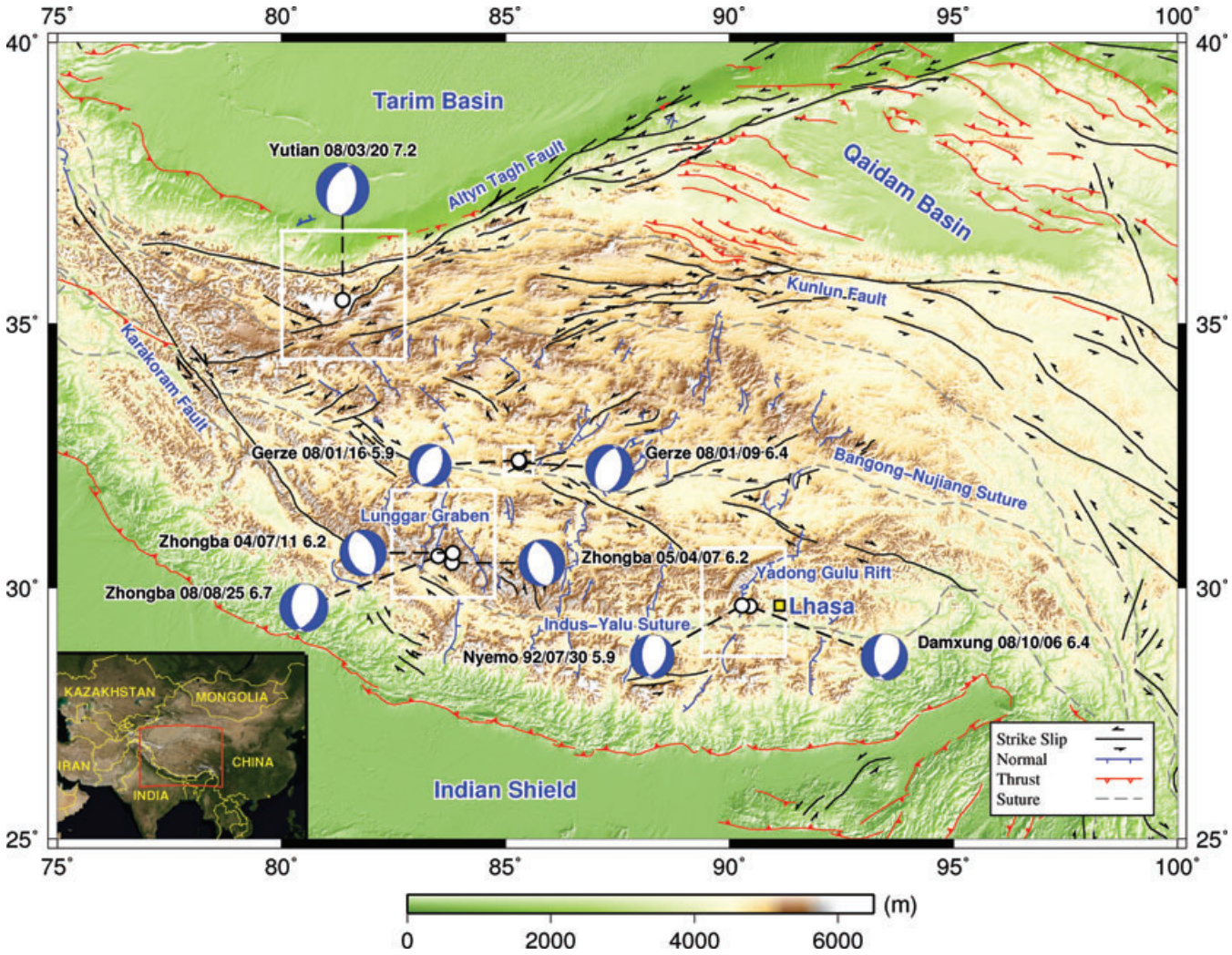

Figure 1. Elevation map of the Tibetan Plateau and immediate surrounding region. The eight normal faulting earthquakes studied are marked by the GCMT focal mechanisms (offset by a dashed line with a white circle to mark their actual location), with the county name, date (yy/mm/dd) and moment magnitude (M_w). Major faults are coloured by type, as indicated in the legend, based upon compilation from Taylor & Yin (2009). White rectangles mark individual topographic maps for each earthquake studied (Figs 3, 6, 10, 15). Inset map shows the region of Asia with the study area delineated in red, and national boundaries marked in yellow.

The five large normal faulting events that occurred in Tibet in 2008 (Fig. 1) represented almost 60 per cent of the moment release from normal faulting earthquakes on the Tibetan Plateau during the past 43 yr (Fig. 2), and are spread across the plateau, being spatially separated by 300–700 km. The normal faulting earthquakes comprise 12 per cent of the total seismic moment release of 1.1×10^{21} N m for this time period. The 2008 January, M_w 6.4, Gerze earthquake occurred in central Tibet, with a large aftershock occurring one week later. The 2008 March, M_w 7.1, Yutian (Keriya) earthquake occurred at the northwestern edge of the Plateau, 50 km south of the Altyn Tagh Fault, and is associated with surface faulting observed in satellite imagery. The 2008 August, M_w 6.7, Zhongba earthquake occurred in southwestern Tibet; this earthquake was preceded by two normal faulting earthquakes of similar magnitude in the area, in 2004 and 2005, which we also examine. The 2008 October, M_w 6.3, Damxung earthquake occurred in southeastern Tibet, close to a similar normal faulting event in 1992 that we also present.

In this paper, we combine interferometric measurements of surface displacements with body wave seismology to determine source mechanisms for the five normal faulting earthquakes that occurred on the Tibetan Plateau in 2008 and the three events prior to 2008 (Table 1). After outlining the methods used in Section 2, we begin by describing the simplest of the normal faulting earthquakes from 2008, namely the M_w 6.3 Damxung earthquake in south-eastern Tibet in Section 3. The subsequent Sections 4–6 describe the larger and more complicated events from 2008. In Section 7, we discuss the contribution these normal faulting events make to crustal thinning and east–west extension of the plateau, and examine the relationship between moment release and surface elevation. We also look at some seismological issues, for example, systematic discrepancies between the InSAR derived fault locations and epicentres in the major seismic catalogues. We also demonstrate that there is no evidence for active low-angle normal faulting amongst these earthquakes. Finally, we address the question of the relationship between surface displacements in the earthquakes and the local geomorphology. The InSAR observations for the three events prior to 2008 are presented in Appendices A and B. The body wave solutions for all the events studied are presented in the on-line supplementary material Appendix C.

© 2010 The Authors, *GJI*
Geophysical Journal International © 2010 RAS

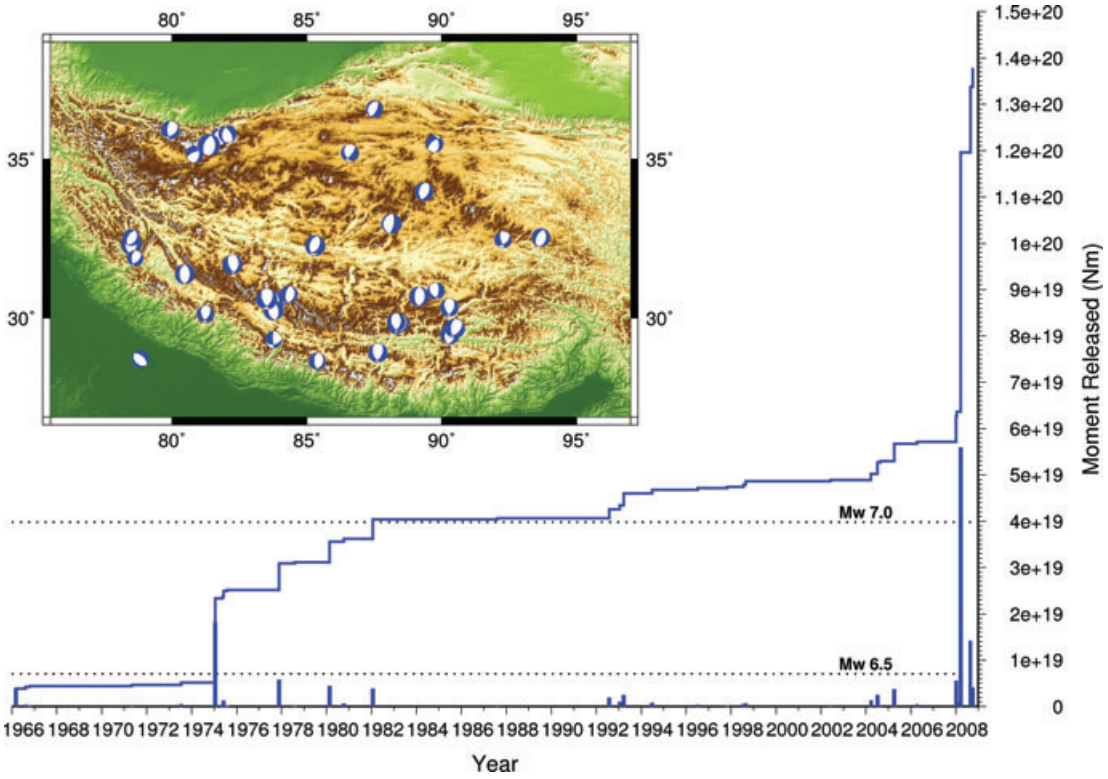

Figure 2. Moment release (blue bars) and cumulative moment release (blue line) from M_w 5.5+ Tibetan normal faulting events recorded in the GCMT catalogue 1976–2008 and a compilation by Molnar & Lyon-Caen (1989). The inset map marks the location of these events in Tibet. The 2008 series of five M_w 5.9+ earthquakes released a total moment more than double the previous four decades of normal faulting seismic events. Note the clustering of events 1992–1993, 2004–2005 and 2008. The moment release from an equivalent individual M_w 7.0 and 6.5 earthquake are marked by dotted black lines.

Table 1. Normal faulting earthquakes on the Tibetan Plateau modelled in this study, listed in order of occurrence. The moment magnitudes (M_w) are from the Global Centroid Moment Tensor (GCMT) catalogue (Ekström *et al.* 2005; Dziewonski *et al.* 1981) and locations are the mid-points of the projection of the fault plane to the surface as determined by InSAR.

Earthquake County	Date (yy/mm/dd)	Magnitude (M_w)	Longitude (°E)	Latitude (°N)
Nyemo	92/07/30	6.1	90.09	29.70
Zhongba	04/07/11	6.2	83.83	30.73
Zhongba	05/04/07	6.2	83.81	30.48
Gerze	08/01/09	6.4	85.35	32.41
Gerze	08/01/16	5.9	85.30	32.45
Yutian	08/03/20	7.1	81.54	35.46
Zhongba	08/08/25	6.7	83.49	30.91
Damxung	08/10/06	6.3	90.43	29.76

2 DETERMINATION OF EARTHQUAKE SOURCE PARAMETERS

2.1 Analysis of SAR interferograms

We used SAR measurements from ascending and descending tracks of the European Space Agency's (ESA) C-Band ENVISAT platform and, in some cases, L-Band SAR data were available from ascending tracks of the Japanese Aerospace Exploration Agency's (JAXA) L-Band ALOS instrument, which augment the range of look angles and number of observations. A single pair of descending ERS-1 SAR acquisitions were used to study the 1992 Nyemo county event. Interferograms were derived from these data using the JPL/Caltech ROI_pac software (Rosen *et al.* 2004), and multilooked to four looks in range and 16 in azimuth (80 m spacing). The interferograms were corrected for differences in satellite position using DORIS satellite orbits from ESA and an empirical baseline refinement was applied. The topographic phase contribution was removed using the 3-arcsec (∼90 m) resolution NASA Shuttle Radar Topographic Mission (SRTM) DEM (Farr & Kobrick 2000).

The interferograms were then filtered using a power spectrum filter (Goldstein & Werner 1998) and unwrapped using the branch cut method (Goldstein *et al.* 1988). Some interferograms required manual unwrapping near the fault because of loss of coherence, or in areas of high relief. The coherence was particularly low in the areas covered by glaciers and snow on the highest ground. Finally, the interferograms were geocoded and rectified to the local UTM coordinate system with an 80 m resolution. We selected SAR acquisition pairs that have the shortest spatial and temporal baselines possible to maximize the interferogram coherence. Additionally, we selected the first suitable acquisition after each coseismic event to minimize perturbation to the co-seismic signal by post-seismic deformation.

Each interferogram yielded several million measurements of ground displacement in the line of sight from the satellite. In order to produce a manageable data set, with the appropriate spatial resolution, we down-sampled the data making use of the high degree of spatial correlation within an interferogram (Hanssen 2001). This reduction was achieved using a quadtree approach (e.g Jonsson *et al.* 2002) which samples the data more heavily in regions of high phase gradient near the fault, except in the case of the Gerze earthquakes where a combination of quadtree and nested uniform sampling was used. The higher density of measurements in the near field reflects

© 2010 The Authors, *GJI*
Geophysical Journal International © 2010 RAS

the greater sensitivity to the mechanism of the earthquake of geodetic observations in this region relative to those in the far field. This procedure gave us ∼500–2000 line-of-sight displacements per interferogram as inputs for our inversion procedure.

For many of the earthquakes studied, interferograms for both descending and ascending passes provide different line-of-sight directions for ground motion. When the numbers of ascending and descending interferograms for a particular earthquake were unequal, we down-weighted interferograms with similar look directions.

All our earthquake mechanisms based on geodetic data treat the ground displacements as being caused by slip on one or more rectangular planes, which are modelled as dislocations within an elastic half-space (Okada 1985). Values for the shear modulus and Poisson's ratio are taken as $\mu = 3.23 \times 10^{10}$ Pa and $\nu = 0.25$, based upon crustal seismic velocities of $V_p = 6.0$ km s^{-1} and $V_s = 3.45$ km s^{-1} (Steck *et al.* 2009), and a crustal density of 2710 kg m^{-3}, which are reasonable given the lack of sediment cover in this region (Bassin *et al.* 2000). We use the same seismic velocities in the body wave inversion for consistency and to allow comparisons between estimates of moment release.

In each case we initially identified the fault position and number of rupture segments from the distribution of interferogram fringes or from digital topography and ASTER imagery (or, in the case of the Yutian earthquake, from the position of surface ruptures and azimuth offsets). We then jointly inverted the interferometric data sets for uniform slip on each fault segment, using a non-linear downhill Powell's algorithm with multiple Monte Carlo restarts to avoid local minima (Press *et al.* 1992; Wright *et al.* 1999). The full set of parameters for each fault segment are: strike, dip, rake, slip, surface centre location, length and top and bottom depth. It was also necessary to solve for the nuisance parameters of a static line-of-sight shift and linear gradients in phase for each interferogram, to account for different unwrapping points and orbital errors. Starting values of the strike, dip, rake and moment of the earthquake were set to those of the Global Centroid Moment Tensor (GCMT) solution. In some cases, it was possible to constrain one or more of the fault parameters by independent observations—or it was necessary to apply constraints to ensure stability of the inversion; these cases are discussed for the individual earthquakes below.

To investigate the limitations of our inversions for uniform slip on the fault segments, we also carried out inversions in which the slip was allowed to vary with position on the fault segments whose geometry is determined from the uniform-slip solution. Each fault segment was subdivided into an array of rectangular elements 1 km in length by 1 km in depth and, following the method of Du *et al.* (1992), Jonsson *et al.* (2002), Wright *et al.* (2003) and Funning *et al.* (2005), we solved for either one (fixed rake) or two (variable rake) components of slip on each segment, and again for the nuisance parameters. A finite-difference Laplacian smoothing constraint was applied to the data in addition to a positivity constraint. We solved the equation,

$$\begin{pmatrix} \mathbf{G} \\ \gamma^2 \nabla^2 \end{pmatrix} \mathbf{m} = \begin{pmatrix} \mathbf{d} \\ 0 \end{pmatrix}, \quad (1)$$

where **G** is the matrix of Green's functions containing the line-of-sight displacement resulting from 1 unit of slip on each element calculated using the elastic dislocation formulation of Okada (1985), ∇^2 is the Laplacian smoothing operator and γ^2 is the smoothing weight factor. The model slip and nuisance parameters are given by **m** and the line-of-sight displacements are **d**. The choice of smoothing factor depends on a compromise between decreasing the fault slip roughness and minimizing the increase in rms misfit that results from the increased smoothing (Wright *et al.* 2004). Following previous authors (Funning *et al.* 2005; Biggs *et al.* 2006), we define the effective length and width of each segment by the contiguous region contained within the contour of slip that contains 95 per cent of the total moment. The average slip and rake is then calculated for that region.

To estimate the uncertainties in fault parameter errors, we perturb the original data sets with random synthetic correlated noise in order to perform a Monte Carlo analysis (Wright *et al.* 2003; Funning *et al.* 2005). In this method, a far-field portion of each interferogram is sampled and the autocovariance function calculated (Hanssen 2001; Lohman & Simons 2005; Wright *et al.* 2004) to which a 1-D covariance model is fitted and used to generate 100 data sets perturbed with noise with the correct statistical properties. We then carry out inversions on each of the data sets and use the sets of individual fault parameters calculated to estimate errors and to examine trade-offs between parameters.

The uncertainties derived from Monte Carlo modelling do not account for errors in our assumptions about choice of fault segmentation, strike, length, location, data sampling or relative interferogram weighting.

2.2 Teleseismic body wave modelling

Teleseismic long-period waveforms for each of the earthquakes are modelled to provide additional constraints for the event source parameters. This is performed using broad-band seismograms from the Global Digital Seismograph Network (GDSN), each of which is deconvolved to give a response equivalent to that of a WWSSN 15–100 s long-period instrument. For each event the MT5 program (Zwick *et al.* 1994) is used to invert *P* and *SH* waveforms for strike, dip, rake, centroid depth, seismic moment and source–time function of the best double-couple solutions. This is done using a weighted least-squares method (McCaffrey & Abers 1988), following the procedure described by Molnar & Lyon-Caen (1989). We model *P*, *pP* and *sP* phases on vertical component seismograms restricted to the epicentral distance range 30°–90°, and *S* and *sS* phases on transverse components in the range 30°–80°, to avoid complications from the Earth's crust and core. Amplitudes are corrected for geometrical spreading, and for anelastic attenuation using Futterman operators with a t^* of 1.0 and 4.0 s for *P* and *SH* waves respectively. We use a simple half-space source velocity model, with velocities, densities and Lamé elastic constants that match those used for the InSAR elastic modelling. A choice of higher velocity of V_p = 6.5 km s^{-1} compared with V_p = 6.0 km s^{-1} results in less than 1 km deepening of the estimate for the centroid depth and approximately 2–10 per cent increase in calculated moment. The minimum misfit solutions for each earthquake are shown in the on-line supplementary material (Appendix C) and are tabulated in each earthquake section with the results from InSAR modelling.

3 THE OCTOBER 2008 DAMXUNG EARTHQUAKE

We present the most recent earthquake first as this event was the most straight forward to model out of those studied. The 2008 October 6, M_w 6.3, Damxung earthquake killed 10 people and injured at least 25, and was felt in Lhasa 75 km to the east (Fig. 1). The largest aftershock (M_w 5.5) occurred 2 d later on October 8 (Fig. 3); this event represents less than 7 per cent of the moment of the main-shock and is neglected in our determination of the parameters

© 2010 The Authors, *GJI*
Geophysical Journal International © 2010 RAS

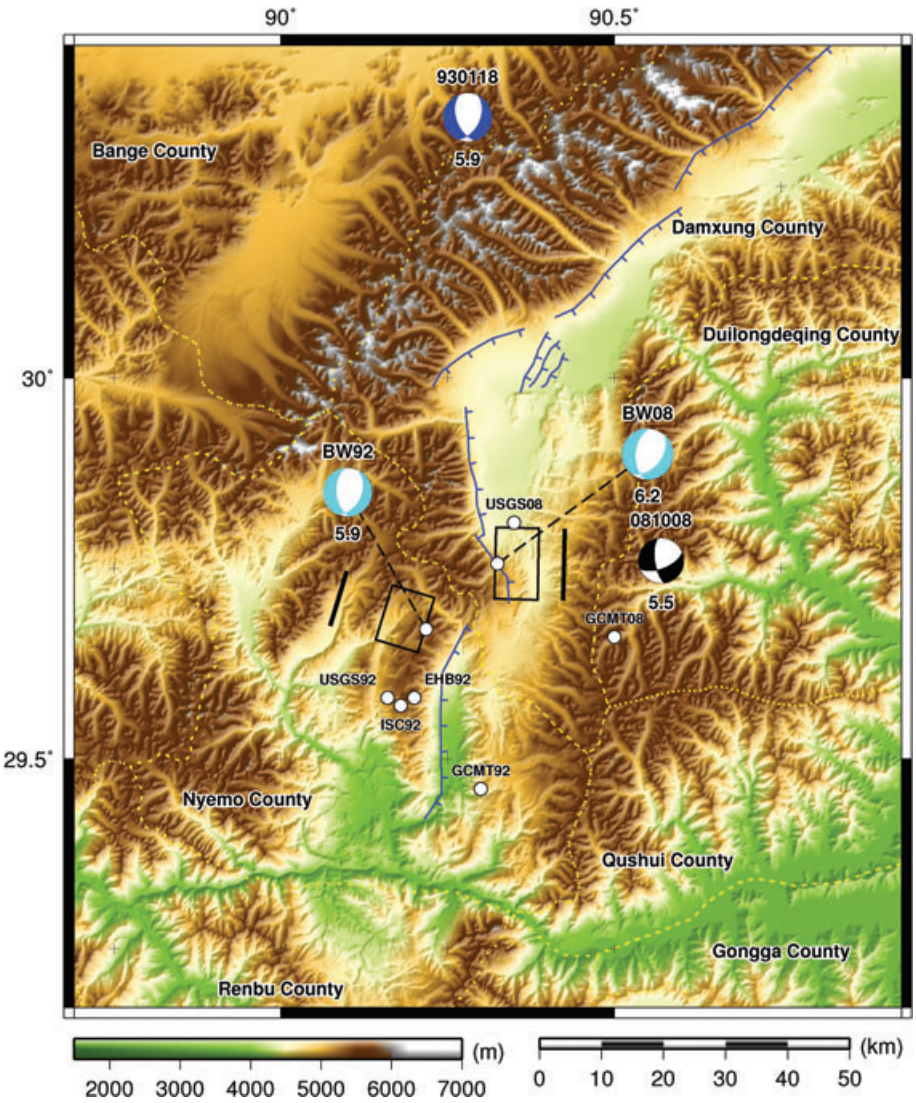

Figure 3. Shaded relief elevation map of the Damxung region, south-eastern Tibet. Surface projections up-dip of fault segments from uniform-slip InSAR modelling of the 1992 and 2008 earthquakes are marked by solid black lines. Fault outlines at depth are marked by black rectangles. Body wave solutions for the two earthquakes are coloured cyan and labelled BW with the year of the earthquake. GCMT centroid, USGS Preliminary Determination of Epicentres (PDE), International Seismological Centre (ISC) and EHB (Engdahl catalogue (Engdahl *et al.* 1998)) locations are marked by white circles. ISC and EHB locations are only available for the 1992 earthquake. GCMT focal mechanisms are given for additional M_w 5.5+ earthquakes (1976–2008) with normal faulting events marked in blue, and strike-slip in black, with dates in yy/mm/dd format above the mechanism and moment magnitude below. Mapped normal faults from Taylor & Yin (2009) are marked in blue. County borders are delineated by dotted yellow lines.

of the main shock. The preliminary centroid moment tensor estimate from the USGS indicated a N–S normal faulting event with a significant strike-slip component, as did that from the GCMT solution. The largest previous earthquake in the immediate area from the GCMT catalogue was a M_w 6.1 event on 1992 July 30, which had a nearly pure dip-slip solution (Fig. 3). This earlier event occurred during the first year of ERS-1 SAR acquisitions, and we have also been able to carry out InSAR and body wave modelling for it (see Appendices B and C).

The Damxung earthquake occurred mid-way along the Yadong Gulu Rift in southern Tibet, (Fig. 1), within which both east- and west-dipping Quaternary normal faults are found (Armijo *et al.* 1986). Kapp *et al.* (2005) mapped high angle normal faults bounding the western edge of the rift, immediately to the north of the Damxung earthquake, but these authors colocate these faults with lower-angle (22°–37°) faults, which they suggest are detachments, still active today at these dips.

3.1 Fault geometry estimated from InSAR

One ascending and one descending pair of ENVISAT SAR passes were of suitable time-span and perpendicular baseline for the co-seismic period of this earthquake (Table 2). The processed interferograms (Fig. 4) show an elongated bulls-eye pattern with maximum line-of-sight displacement of 30 cm corresponding to hanging wall subsidence. Uplift of the footwall is seen in the descending interferogram as a 5 cm range decrease. However, the combination of this uplift and eastward motion in the footwall is manifested as motion away (∼3 cm) in the ascending interferogram due to the look angle.

The projection of the modelled fault to the surface is positioned between the region of subsidence and slight uplift, just to the east of the highest deformation gradient. Initially we inverted the data sets with all fault parameters free for uniform slip on a single fault segment, but the solutions all yielded high slip on a narrow width fault, approximating the slip as a buried line source. We therefore

© 2010 The Authors, *GJI*
Geophysical Journal International © 2010 RAS

Table 2. Details of interferograms for the M_w 6.3 2008 October 6 Damxung earthquake. Columns show ENVISAT tracks, satellite directions (ascending or descending), incidence angle (°) in the centre of the scene, dates of SAR frames, time interval ΔT, post-seismic interval ΔPT, and perpendicular baseline $B_\perp$. The perpendicular baseline is the average of the top and bottom perpendicular baseline in the interferogram. The variance (σ^2) and e-folding length scale (Distance) are those calculated from the covariance function of interferogram noise and are used the Monte Carlo estimation of fault parameter errors. The number of data points used in the inversion, the relative weighting for each of the data sets and the weighted rms for the uniform slip and distributed slip (fixed and variable rake λ) inversions are also given.

Satellite	Track no.	Direction (asc/dsc)	Incidence (°)	Master (yy/mmd/d)	Slave (yy/mm/dd)	ΔT (dys)	ΔPT (dys)	$B_\perp$ (m)	σ^2 σ^2 (cm^2)	Distance (km)	Data (pts)	Weight	RMS (cm)		
													Uniform	Fix λ	Vary λ
Env	176	dsc	23	08/09/21	08/10/26	35	20	231	0.32	7.2	1006	1	1.1	1.1	1.0
Env	26	asc	41	08/04/23	08/10/15	175	9	61	0.21	7.6	1004	1	1.3	1.2	1.1

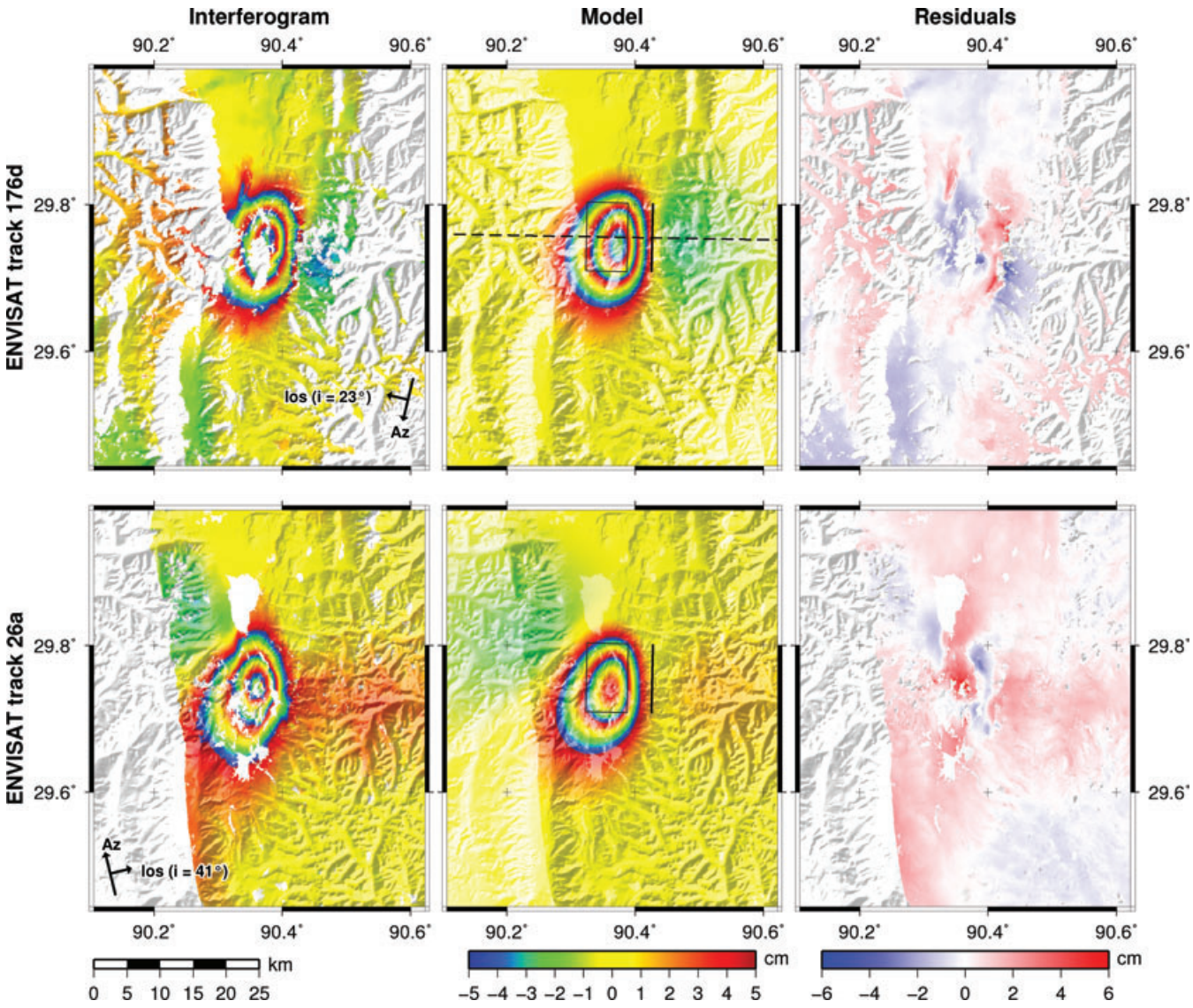

Figure 4. Damxung 2008 October 6 earthquake interferograms with uniform slip modelling. Interferogram and model show range changes as fringes rewrapped to 10 cm, with colour cycles blue to red indicating motion away from the satellite. Residuals are unwrapped values for clarity. The fault segment is marked by a solid black line, with the black box indicating the outline of the fault at depth projected to the surface. Satellite track azimuth (Az) and line-of-sight (LOS) with angle of incidence (i) are indicated by black arrows. The black dashed line indicates the location of the profile shown in Fig. 24 in Section 7.

fixed the slip in 0.1 m intervals between 0.1 and 2.0 m and ran the inversion with all other parameters free. The rms misfit between the model and interferograms decreases with increasing slip, but the improvement is imperceptible for slips above 1 m (Fig. 5), and we therefore fixed the slip to 1 m.

The best-fitting solution for each parameter for the uniform, fixed slip model is given in Table 3 along with the estimated error associated with each, based on inversions of 100 sets of interferogram data perturbed with characteristic noise (the noise variance is given in Table 2). The best-fitting model indicates a north–south

© 2010 The Authors, *GJI*
Geophysical Journal International © 2010 RAS

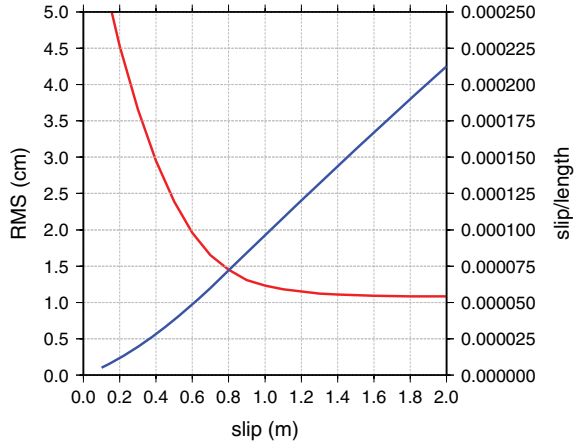

Figure 5. Rms misfit (red line) versus magnitude of slip fixed in solving for the Damxung fault geometry. Improvement in fitting the interferogram data becomes insignificant for choices of uniform slip above ∼1 m, with slip-to-length ratios (blue line) also increasing.

striking, westward dipping normal fault with moderately oblique right-lateral slip. The rupture does not reach the surface, extending from a depth of 11 km up to 4 km on a 10 km long fault. The rms misfit for the descending track was 1.1 cm and slightly more, 1.3 cm, for the ascending (Table 2), whereas fixing the slip at 0.6 cm increased the rms to almost 2 cm in both data sets. The low uncertainty in fault parameters from Monte Carlo analysis results from fixing the fault slip, which reduces the trade-off between parameters. However, varying the choice of fixed slip value between 0.6–1.5 m changes strike, dip and rake estimates by ±1°, ±3°, ±5°, respectively and fault extents by ±1 km. The fault position varies by less than half a kilometre. No significant improvement in residuals arose from allowing variable slip on the fault planes (Table 2).

3.2 Teleseismic body wave modelling

Teleseismic body wave modelling as described in section 2 yields the fault parameters given in Table 3 and the minimum misfit solutions for *P* and *SH* waves are given in the on-line Appendix C. The solution yields a N–S striking, 51° westward-dipping fault with a centroid depth of 7 km, and a moderate component of right-lateral slip.

There is very close agreement between the InSAR solutions and that from the body wave modelling. The estimated seismological source dimensions are also in close agreement with the InSAR models, with buried slip from 3 to 12 km. However, the calculated moment from the body wave solution is about 10 per cent lower than that calculated from the InSAR for uniform slip, which in turn is 10 per cent lower than that given by the USGS (Table 3); the GCMT solution is a further 10 per cent higher than that of the USGS.

3.3 Summary

The surface deformation of the 2008 M_w 6.3 normal faulting earthquake in Damxung county can be modelled simply with a uniform elastic dislocation model of a north–south striking fault, dipping westward at 45°, and rupturing between depths of 4 and 11 km. The body wave solution yields a very similar solution to the InSAR. The slip on the fault is not modelled as reaching the surface, but the surface projection of the fault is associated with the west flank of a north–south mountain range, and westward dipping faults as mapped by Armijo *et al.* (1986). The location of subsidence in the InSAR is partially beneath the high topography on the western edge of the rift (Fig. 3). We note the discrepancy between the InSAR earthquake location and the seismological locations (in particular that of the GCMT solution) and we examine this for all earthquakes in Section 7.

An earlier M_w 5.9 normal faulting event occurred in 1992, 20 km WSW of the 2008 earthquake (Fig. 3), also beneath the more mountainous topography. InSAR and body wave modelling for this earthquake are shown in Appendices B and C.

4 THE 2008 JANUARY GERZE EARTHQUAKES

On 2008 January 9, a M_w 6.4 earthquake hit Gerze and Nima Counties in western central Tibet (Figs 1 and 6). Two large aftershocks measuring M_w 5.9 and M_w 5.5 followed on January 16 and 22, respectively, and the region experienced around 30 smaller ($M_w <$ 5.0) teleseismically recorded aftershocks between the main shock and the end of January. No fatalities were recorded, but the earthquake affected ∼2000 people, causing economic losses estimated at 4 million yuan (∼US $500 000).

The teleseismic hypocentres for the Gerze earthquakes (GCMT and USGS, see Fig. 6) are clustered near the southern termination

Table 3. Damxung fault parameters from inverting interferometric data, from *P* and *SH* body wave modelling, and as listed in the Global CMT and USGS catalogues. The latitude and longitude are for the up-dip projection of the fault centre to the surface for InSAR models, the centroid location for GCMT and the hypocentre for the USGS solution. Top and bottom refer to the top and bottom depths of the fault plane, and Centroid is the centroid depth. Errors stated for the InSAR uniform slip model (InSAR-u) are 1 sigma values from the result of Monte Carlo error analysis. The InSAR distributed slip model is given for a fixed rake (InSAR-d-fr) and variable rake (InSAR-d-vr), where the fault geometry is fixed to that from the uniform slip model and the fault length and width are given by the contoured region containing 95 per cent of the total moment released, with the average slip then calculated for this contoured area. For the seismological body wave solutions, the slip, length, top and bottom depth are estimated by calculating a source dimension from the centroid depth and moment. This assumes a square fault with a fixed slip-to-length ratio of 5×10^{-5}. Therefore, the length scales as the cube root of the moment, $M_0 = 5 \times 10^{-5}\ \mu L^3$, where μ is the rigidity equal to 3.2×10^{10} Pa.

Model	Strike (°)	Dip (°)	Rake (°)	Slip (m)	Longitude (°)	Latitude (°)	Length (km)	Top (km)	Bottom (km)	Centroid (km)	Moment, M_0 $\times 10^{18}$	M_w
InSAR-u	181 ±1	47 ±1	245 ±2	1.0 fixed	90.43 ±0.1 km	29.76 ±0.1 km	10.4 ±0.2	4.0 ±0.1	10.7 ±0.2	7.4 ±0.1	3.1 ±0.1	6.2
InSAR-d-fr	181	47	245	0.58	90.43	29.76	17	4	13	8	3.3	6.2
InSAR-d-vr	181	47	231	0.38	90.43	29.76	25	4	14	7	3.9	6.3
Body wave	185	51	247	0.6			12	3	12	7	2.8	6.2
GCMT	178	53	238		90.50	29.66				12	3.7	6.3
USGS	180	48	241		90.35	29.81				12	3.4	6.3

© 2010 The Authors, *GJI*
Geophysical Journal International © 2010 RAS

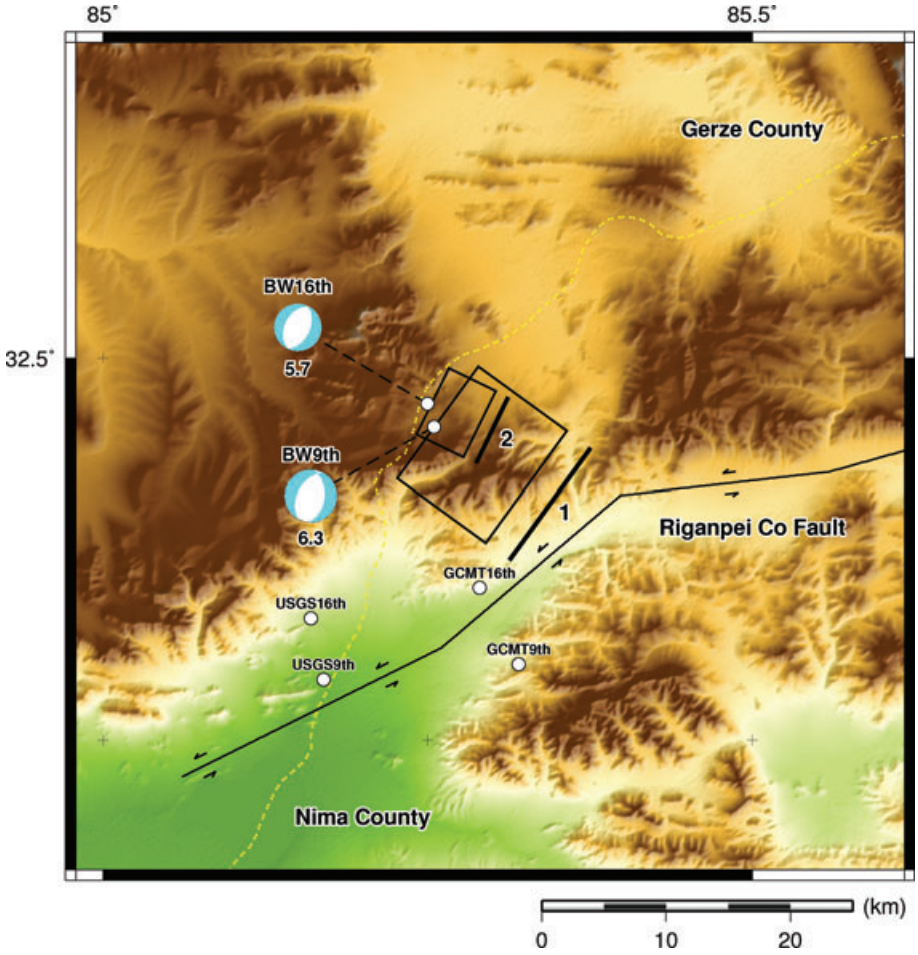

Figure 6. Shaded relief elevation map of the Gerze region, central Tibet. The numbers 1 and 2 refer to the two different fault segments. Symbols as for Fig. 3.

Table 4. Details of interferograms for the Gerze M_w 6.4 earthquake 2008 January 9; details as for Table 2.

Satellite	Trac no.	Direction (asc/dsc)	Incidence (°)	Master (yy/mm/dd)	Slave (yy/mm/dd)	ΔT (dys)	ΔPT (dys)	$B_\perp$ (m)	σ^2 (cm^2)	Distance (km)	Data (pts)	Weight	RMS (cm)		
													Uniform	Fix λ	Vary λ
Env	348	dsc	23	07/11/23	08/02/01	70	23	8	0.098	5.9	1942	1.0	2.5	2.2	2.2
Env	427	asc	41	07/03/28	08/02/06	315	28	22	0.015	3.3	1940	0.5	1.4	1.2	1.0
ALOS	509	asc	39	07/10/16	08/01/16	92	7	493	0.386	1.0	1917	0.5	2.1	1.5	1.4

of the left-lateral Riganpei Co fault (Fig. 6). The Riganpei Co fault defines the southern end of the northeast striking Yibug-Caka fault zone, which Taylor *et al*. (2003) infer to be the left-lateral half of a pair of conjugate strike-slip fault zones. These authors propose that many such pairs make up a conjugate fault zone that accommodates east-west extension across central Tibet and links extensional rift systems north and south of the Bangong-Nujiang suture zone Fig. 1). Seismic fault plane solutions for the main shock and aftershocks show normal faulting mechanisms striking NNE–SSW for all events, with minor strike-slip components. Sun *et al*. (2008) inverted interferograms derived from ENVISAT data and found that the observed deformation patterns are consistent with normal faulting on two NW-dipping subparallel faults.

4.1 Fault geometry estimated from InSAR

Repeated radar acquisitions are available for two ENVISAT tracks with ascending and descending viewing geometries, and one ALOS track with ascending viewing geometry (Table 4). Both ENVISAT acquisition pairs span the three largest earthquakes, whilst the ALOS acquisition pair spans only the first two events.

The deformation signal for the descending track interferogram shows two lobes and is consistent with a normal fault striking ∼NE–SW and dipping to the west (Fig. 7, left-hand panels). The deformation signals for the ENVISAT and ALOS ascending track interferograms both show a strongly asymmetric three-lobe pattern. In all three interferograms, the lobe with the highest deformation gradients has two distinct minima of line-of-sight deformation, each of around 0.4 m displacement away from the satellite.

Attempts to down-sample the data using the quadtree method failed to capture the three-lobe deformation pattern with high enough resolution. Therefore we sampled only the central deformation lobe with the quadtree method, sampling the remaining near-field at a regular spacing of 1.5 km, and the far-field at a regular spacing of 4.5 km. The ENVISAT and ALOS ascending data sets

© 2010 The Authors, *GJI*
Geophysical Journal International © 2010 RAS

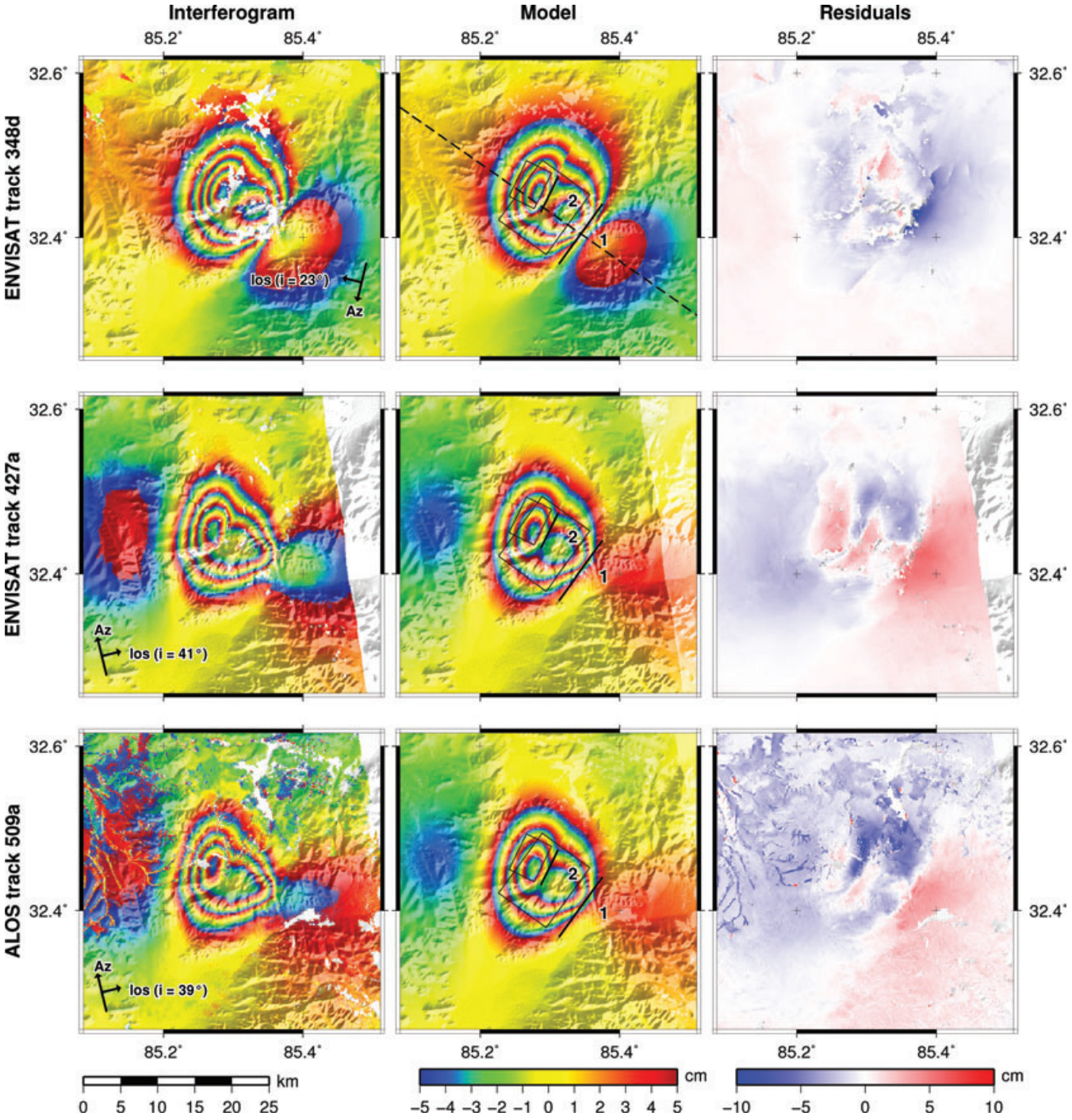

Figure 7. Gerze earthquake interferograms for distributed slip modelling with a fixed rake. The numbers 1 and 2 refer to the two different fault segments. Symbols as for Fig. 4.

display similar look geometry, and so during the inversion process we chose to down-weight each of these data sets to 1/2 the weight of the descending ENVISAT data set.

Inversions with uniform slip on a single fault failed to match the double minima pattern of the data interferograms and resulted in a large rms misfit. This poor fit is likely to be due to the observed signal combining at least two separate events, probably occurring on separate faults. GCMT and our body wave solutions suggest that the moment of the largest aftershock makes a significant contribution to the total deformation signal (up to 14 per cent). In comparison, the moment sum of the January 22 M_w 5.4 aftershock and all smaller aftershocks only makes up ∼4 per cent of the total seismic moment release recorded in the interferograms, so we choose to neglect these during modelling. From forward modelling experiments, it is evident that the pattern with two minima can be reproduced only by incorporating a second westward-dipping normal fault situated in the hanging-wall of the main fault. It was not possible to isolate the signals from the two main earthquakes and so we had to invert the data for two faults simultaneously. Inversions with slip and length free to vary resulted in solutions for the two earthquakes approximating line sources, with high slip on faults with very narrow length or width. Therefore, we fixed the length of the primary

© 2010 The Authors, *GJI*
Geophysical Journal International © 2010 RAS

Table 5. Fault plane parameters for the Gerze earthquakes from inverting interferometric data, from *P* and *SH* body wave modelling, and as listed in the Global CMT and USGS NEIC catalogues. Caption as for Table 3.

Model	Strike (°)	Dip (°)	Rake (°)	Slip (m)	Longitude (°)	Latitude (°)	Length (km)	Top (km)	Bottom (km)	Centroid (km)	Moment, M_0 $\times 10^{18}$ (Nm)	M_w
2008 January 9 earthquake												
InSAR-u	223	51	293	1.18	85.34	32.40	10.0	3.1	14.5	8.8	5.65	6.4
	±12	±4	±6	fixed	±1.2 km	±1.5 km	fixed	±1.0	±2.8	±0.9	±1.9	
InSAR-d-fr	223	51	293	0.95	85.34	32.40	13	0	12	6	4.68	6.3
Body wave	208	47	286	0.7			14	1	11	6	4.46	6.3
GCMT	206	46	285		85.32	32.30				13.3	5.0	6.4
USGS	204	43	297		85.17	32.29				7	3.0	6.2
2008 January 16 earthquake												
InSAR-u	206	54	273	0.87	85.30	32.45	5.3	1.6	5.0	3.3	0.63	5.8
	±17	±10	±12	fixed	±2.5 km	±2.1 km	fixed	±1.6	±0.7	±1.0	±0.2	
InSAR-d-fr	206	54	273	0.30	85.30	32.45	10	1	6	3.5	0.96	5.9
Body wave	206	43	271	0.35			7	2	6	4	0.52	5.7
GCMT	198	46	267		85.29	32.35				12	0.87	5.9
USGS	220	50	306		85.16	32.33				5	0.4	5.6

fault to 10 km estimated from the ∼4 s source–time function from the body wave modelling results (Appendix C). The length for the secondary fault was fixed at 5.3 km according to scaling relationships (Scholz 2002) based on the ratio of the earthquakes' scalar moments from the body wave analysis. We also fixed the ratio between slip values for the two faults in the same way. The data were then inverted several times, fixing the slip over a range of values as for the Damxung earthquake but keeping the same relative slip ratio between the faults. We selected a slip of 1.2 m for the primary fault (and therefore 0.56 m for the secondary fault) for the best model, based on the rms minimum. We then fixed the strike, length, location and dip of both faults from this model, and inverted for slip, rake and top and bottom fault depths. This allowed the slip to vary and as a result the slip on the secondary fault increased to around ∼0.9 m whilst slip on the primary fault remained at around 1.2 m. All other parameters remained unchanged, except the bottom depth on the secondary fault, which decreased by 1.5 km, and the top depth, which increased by 0.5 km.

The InSAR model shows that the main fault strikes NE–SW and dips to the NW, with a rake of 293° indicating a small left-lateral component to the dip-slip. The largest aftershock occurred on a smaller synthetic normal fault sub-parallel to the primary fault and situated in its hanging-wall. The solution is consistent both with seismic models of the earthquakes (Table 5) and with remote sensing observations of the hypocentral area. The surface projections of both fault planes correspond to elongate patches of incoherence in both ENVISAT interferograms, particularly for the descending track (Figs 7 and 8), likely to be caused by ground movement at the surface projection of the faults during the earthquakes. The surface projection of the main fault also approximates surface features seen in ASTER imagery, with triangular facets, a sharp break in slope, and a change in drainage marking the fault trace (Fig. 8). The model fault trace appears to represent the average strike of the mapped surface trace. In contrast, the surface projection of the modelled second fault is associated with no clear surface features.

We estimate model parameter uncertainties using the Monte Carlo method detailed in Section 2. The results of this analysis show that the 1σ errors for the majority of fault parameters for both faults are fairly large. This is likely to be due to trade-offs between parameters for the main fault and parameters for the secondary fault, resulting from our inversion for both faults simultaneously. The magnitude of these errors is supported by the results of varying the choice of fixed slip value. Varying the primary fault slip between 0.8 and 1.3 m (and also varying slip on the corresponding secondary fault accordingly), gives ranges for the strike, dip and rake estimates of 22°, 12°, 23°, respectively on the main fault, and 4°, 6°, 12°, respectively on the secondary fault. The fault positions vary by less than one and a half kilometres.

The rms misfit for the uniform-slip model is small (<2.0 cm), but there are still large residuals locally, showing that it is not possible to reproduce significant features of the observed surface deformation by uniform slip. We next modelled the earthquakes by fixing the geometry of the faults and inverting for variable slip on an array of 1 km length by 1 km depth fault patches on each fault plane. The surface deformation resulting from the best-fitting model is shown in Fig. 7. The rms misfit from the model is 1.7 cm and residual interferograms have a maximum of ∼10 cm unmodelled deformation (Fig. 7). The slip distribution shown in Fig. 9 has a maximum slip of almost 2.0 m at a depth of 7–8 km. The maximum slip in the top kilometre is 12 cm, representing the magnitude of displacements expected at the surface. The uniform-slip solution yields a fault plane that is of shorter length than the maximum length of the distributed-slip model, and is buried to a depth of ∼3 km. This is probably the main reason for the difference in misfit between the uniform and distributed slip models (2.0 cm *versus* 1.7 cm, respectively). The area of the variable-slip fault plane that contains 95 per cent of the total slip is of similar size to that of the uniform-slip fault. Although maximum slip on the fault is higher than slip in the uniform model, the average slip on the distributed model is lower, with a slip-length ratio that falls within the empirical bounds for most earthquakes ($1 \times 10^{-4} - 2 \times 10^{-5}$, Scholz 2002). The slip distribution on the secondary fault is elliptical, with a maximum slip of 0.9 m at a depth of 3–4 km. The maximum slip in the top km is 9 cm. We find that there are small but significant amounts of slip in the top kilometre (i.e. at the surface) for both faults. A second inversion was performed with both rake and slip allowed to vary between fault patches. The solution did not reduce the misfit to the data significantly, and added unnecessary complication to the model, and so is not presented here.

4.2 Teleseismic body wave modelling

The fault parameters from body wave modelling for both of the 2008 Gerze earthquakes are given in Table 5 and the minimum misfit

© 2010 The Authors, *GJI*
Geophysical Journal International © 2010 RAS

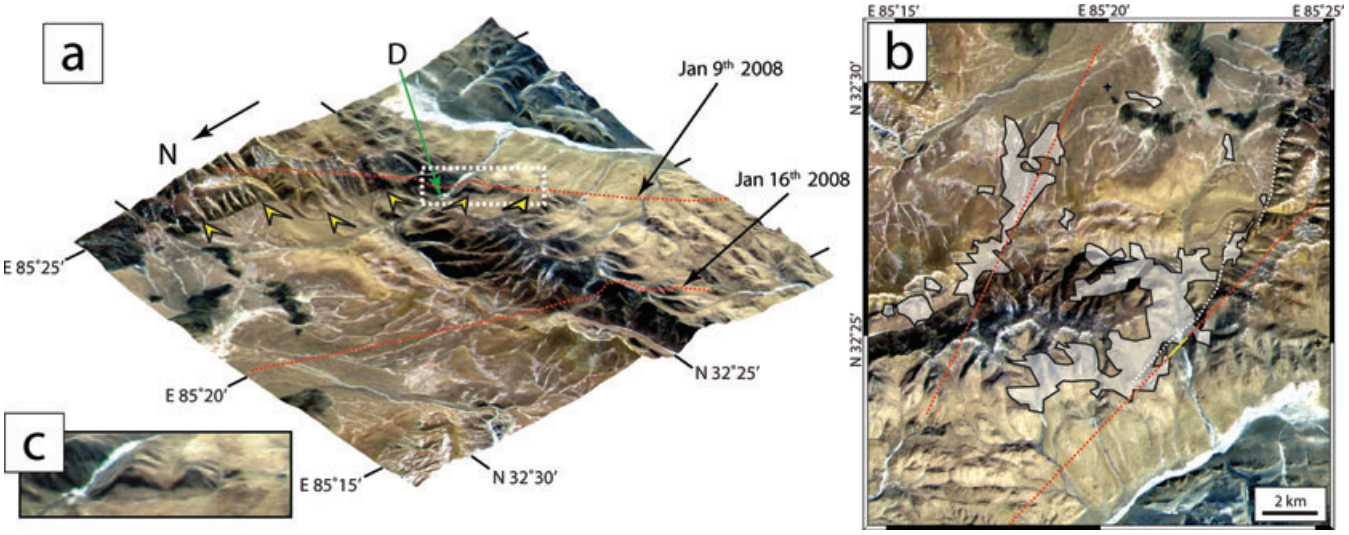

Figure 8. Preseismic ASTER satellite image (bands 321) of hypocentral region acquired on the 2006 March 19. Perspective image (a) viewed from the NW shows surface features associated with the fault that ruptured during the January 9 earthquake (yellow arrows). Red dashed lines mark the surface projection of the fault planes extended from the uniform-slip inversion (note that the main fault extends off the edge of this image to the SW by several km). D shows a river whose drainage is interrupted across the main fault. To the west of this feature are two well-defined triangular facets along the main fault [a magnified view of the features inside the white dashed box, including these triangular facets, can be seen in panel (c)]. A change in incision and a break in slope are also used to define the fault here and further to the NE. This fault is indicated in map view (panel b) with a white dashed line. The fault runs almost N–S in the north of the region, then steps to the right to a new segment which moves around to strike SW further to the south. Red dashed lines are the same as for the perspective view, and superimposed yellow line shows the segment of the main fault that has >10 cm of slip in the top one kilometre from the variable-slip model. The semi-transparent white regions are incoherent areas in the descending track ENVISAT interferogram.

solutions for *P* and *SH* waves are given in the on-line Appendix C. For the primary fault the body wave solution yields a NE–SW striking, 47° NW-dipping fault with a centroid depth of 6 km, and a small component of left-lateral slip. For the secondary fault the solution gives a fault plane parallel to the main fault, but with a purely normal sense of slip and a shallower centroid depth of 4 km.

For both faults there is close agreement between the InSAR solutions and that from the body wave modelling for most parameters, but there is a discrepancy between the InSAR and body wave estimates of strike on the main fault. The InSAR model gives a strike of 223° for the fault plane, whereas the body wave modelling gives a strike of 208°. However, the strike from the body wave analysis is within the two sigma InSAR error bounds of ±24°. The calculated moments for the main fault and the secondary fault are about 5–10 and 40–45 per cent (respectively) lower than that calculated from the InSAR and that given by the GCMT (Table 5); the USGS moments for both earthquakes are ∼30 per cent smaller than our body wave estimates.

4.3 Summary

The M_w 6.4 and 5.9 Gerze earthquakes on the central Tibetan Plateau principally involved NW dipping normal faulting on two previously unknown faults with maximum slips of 2.0 and 0.9 m and a small left-lateral slip component on the primary fault. These normal faults are probably kinematically linked with the left-lateral Riganpei Co fault and the fault plane of the larger earthquake in particular terminates close to or against the Riganpei Co fault.

5 THE 2008 MARCH YUTIAN EARTHQUAKE

On the 2008 March 20 at 22:33 UTC (06:33 March 21, local time), a M_w 7.1 earthquake struck the southern edge of Yutian county, 150 km due south of Yutian, on the Xinjiang–Xizang (Tibet) border, China (Fig. 1). No fatalities were recorded, but the earthquake affected ∼100 000 people, damaging 30 000 houses and causing an estimated 300 million yuan (40 million US dollars) of economic losses. No aftershock above M_w 5.6 has occurred in the region since the main shock (Fig. 10). The largest recorded previous normal faulting earthquake in the area was a M_w 5.8 event which occurred 50 km to the NE in 1980.

The Yutian earthquake occurred on a north-south trending graben that strikes perpendicular to the left-lateral Altyn Tagh Fault 50 km to the north. Here the Altyn Tagh Fault changes from a SW to WNW strike at the southern limit of the rigid Tarim Basin (Fig. 1); recent InSAR measurements indicate a slip rate on this fault of 5–10 mm yr^{-1} (Wright *et al.* 2004; Elliott *et al.* 2008). This graben forms one of the most northerly regions of normal faulting on the Tibetan Plateau and has the highest elevation in the world of almost 6 km when averaged over a length-scale of 100 km. To the immediate south is the ENE striking Longmu–Gozha Co strike-slip fault which is structurally linked to the Altyn Tagh Fault (Raterman *et al.* 2007) and was initially mapped by Armijo *et al.* (1986), as was the normal fault studied here. Recent earthquakes show a mixture of north–south striking normal faulting and NE–SW striking strike-slip faulting, assuming a left-lateral sense of slip sympathetic to the Altyn Tagh (Fig. 10).

5.1 Fault location

The fault location is clearly seen in the topography, with an obvious west-facing mountain front that reaches an elevation of ∼6700 m (Fig. 10). The initial GCMT solution for this earthquake had one plane striking SSE at a moderate-to-steep dip (Table 7). Azimuth offsets were derived for ENVISAT tracks 155 ascending and 477 descending (Fig. 11). Because of their level of noise, these data were not used in the inversions for fault parameters but, in

© 2010 The Authors, *GJI*
Geophysical Journal International © 2010 RAS

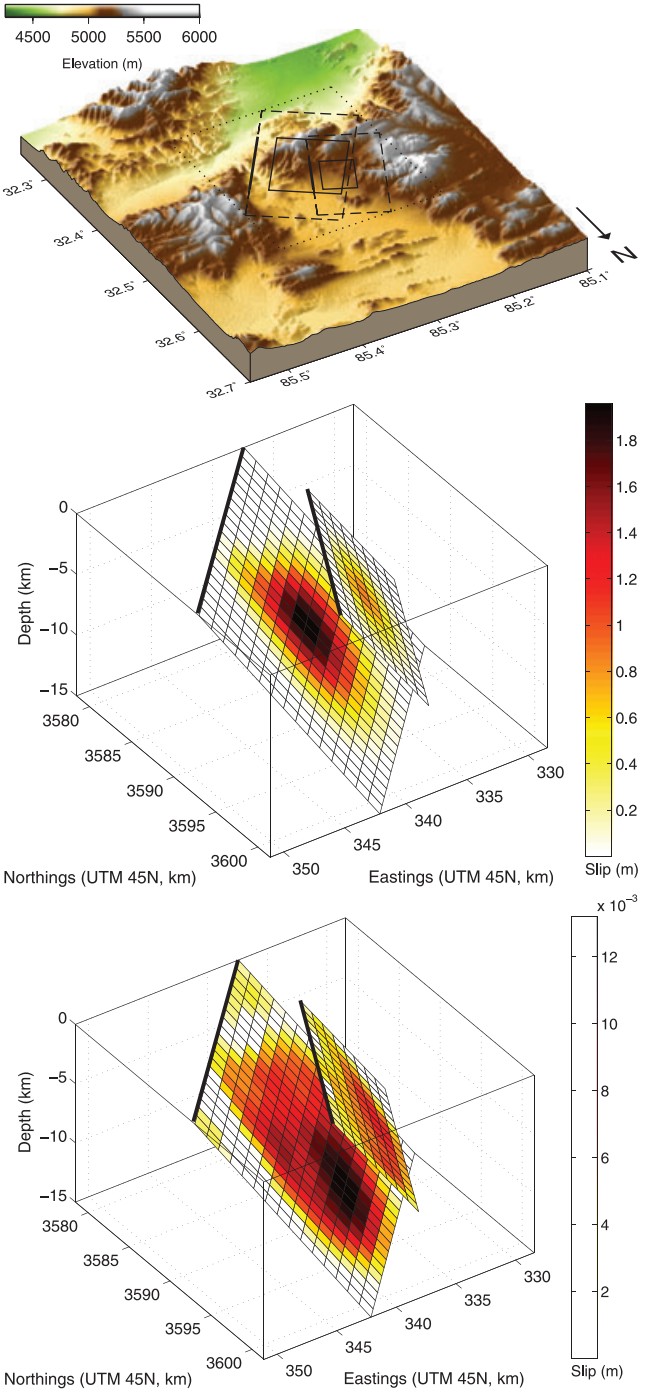

Figure 9. Gerze earthquakes slip distribution with fixed rake based upon the fault orientation from uniform slip modelling. Top: topography with fault trace at surface marked by the thick black line and the outline of the fault at depth by the thin black line – solid for uniform slip, dashed for distributed slip. The dotted line is the outline of the box from the lower two panels. Middle: distribution of slip for the two fault planes. Maximum slip is 2.0 m for the main fault and 0.9 m for the secondary fault. Bottom: 1σ errors in slip, estimated from inverting 100 perturbed data sets created by adding characteristic noise to the original interferograms, increase with depth for both faults, but do not exceed 1.5 cm on either fault. Tables of inferred fault slip on the individual fault patches can be found in the on-line supporting information.

conjunction with the ASTER imagery, they constrain the location and segmentation of the faults. The change in sign of the offsets on both tracks shows clearly that the most northerly fault segment strikes to the NNE. Track 155 shows over 1 m of SSE motion parallel to the mid-fault segment in the hanging wall (Fig. 11, left-hand panel) and track 477 shows over 1 m motion to the SSW.

An ASTER satellite image, acquired one month after the earthquake (2008 April 21) shows clear surface breaks in the glaciated parts of the image, in the centre and to the south of the well defined topographic mountain front (Fig. 12). The surface breaks run approximately northeast–southwest in the southern portion and north–south in the central section and are seen to extend over a distance of 20 km. These features are not seen in an image acquired 3 months prior to the earthquake (Fig. 12, left-hand images). We attribute these features to coseismic surface breaks indicating rupture from depth up to the surface. These observations are crucial in constraining the *a priori* location, strike and segmentation of the fault, in addition to indicating that significant slip at the surface is very likely to have occurred. The surface breaks parallel the overall topographic mountain front and strike 167° in the north and 200° in the south.

Based upon these observations, we treat the earthquake as occurring on three separate fault segments as delineated in Figs 10 and 13.

5.2 Fault geometry estimated from InSAR

The area of surface deformation associated with this earthquake is a couple of hundred kilometres across in an east-west direction, and therefore requires interferograms from several adjacent tracks, each of which is typically 70–100 km wide. Two descending ENVISAT tracks and six ascending tracks consisting of ENVISAT and ALOS acquisitions with varying look angles have suitable acquisitions for forming interferograms (Table 6).

Each of the interferograms covering the fault shows clear line-of-sight displacements away from the satellite in the hanging wall (Fig. 13). The interferogram for ALOS ascending track 514 shows up to 10 fringes with 20 cm spacing indicating 2 m of movement away from the satellite for the central part of the fault. The coherence in the interferograms is poor for the region of the most southern fault segment, with the two L band ALOS tracks having the best interferogram coverage. The poor coherence in the west and in the immediate footwall is due to the glaciated topography above 6000 m (Figs 10 and 12), which results in temporal decorrelation in the interferometry. In the northern central part, the interferogram fringes run approximately north–south in the hanging wall, before turning east–west for the most northern part. The footwall fringes show a clear lobe pattern which is elongated NNE–SSW, where they run parallel to the topographic front in the south. To the west of the main lobe associated with hanging wall subsidence, the ENVISAT ascending interferogram shows a lobe with motion towards the satellite (Fig. 13).

We fix the strike and fault surface location of the central segment (labelled 2 in Fig. 10) from the ASTER fault ruptures and topography. We constrain the most southerly segment (number 3) to start at the point the surface ruptures change from north–south to striking SSW, and to join the central segment at the surface. We terminate the southern end of the third fault segment just beyond the end of the mapped surface ruptures where the prominent ridge in the topography also dies out (Fig. 12, box c). The strike and location of the northern segment (number 1) is constrained from the discontinuity in azimuth offsets (Fig. 11) and from the fringe patterns of the

© 2010 The Authors, *GJI*
Geophysical Journal International © 2010 RAS

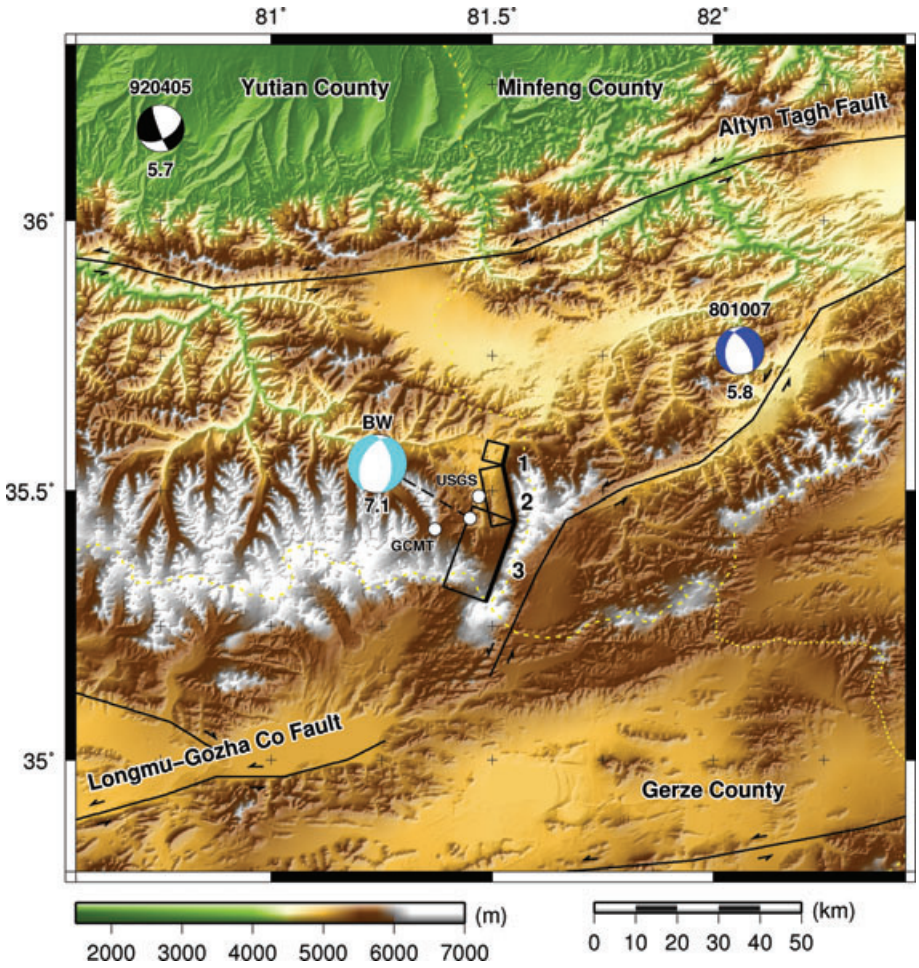

Figure 10. Shaded relief elevation map of the Yutian region, northwestern Tibet. The left-lateral Altyn Tagh and Longmu–Gozha Co faults are marked in black. The fault bounded mountains in the footwall of the Yutian earthquake rise to 6736 m, over 1 km above the hanging wall. This region has the highest topography averaged over a 100 km length-scale in the world. Rest of caption as for Fig. 3.

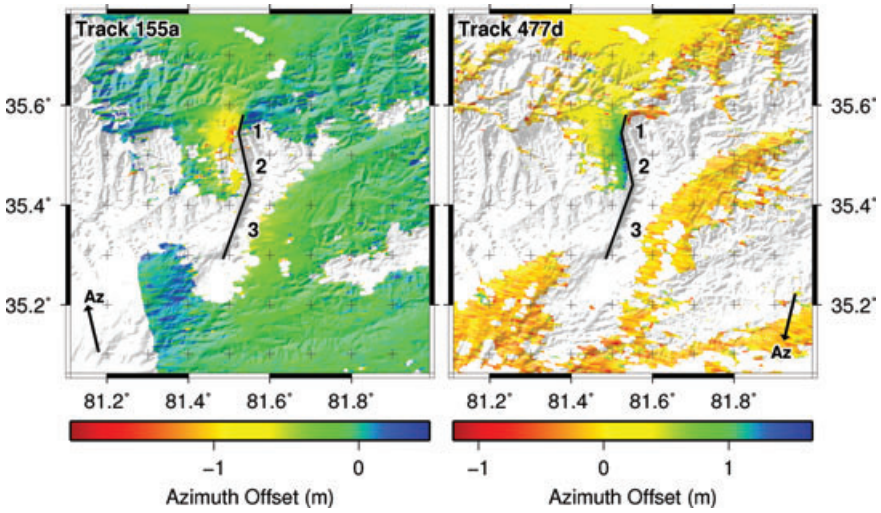

Figure 11. ENVISAT azimuth offsets for ascending track 155 (left-hand panel) and descending track 477 (right-hand panel). The calculated offsets are noisy in the glaciated regions, and have been masked out. The azimuth direction (Az) is marked by a black arrow, and the three fault segments by black lines, numbered to match those listed in Table 7. Over 1 m of motion to the SSE is shown in the ascending offset data (left-hand panel) and similarly over 1 m of motion to the SSW in the descending track (right-hand panel). The change in offset direction is clearly shown for the most northerly fault segment, and provides a useful constraint for the location and strike of this segment.

© 2010 The Authors, *GJI*
Geophysical Journal International © 2010 RAS

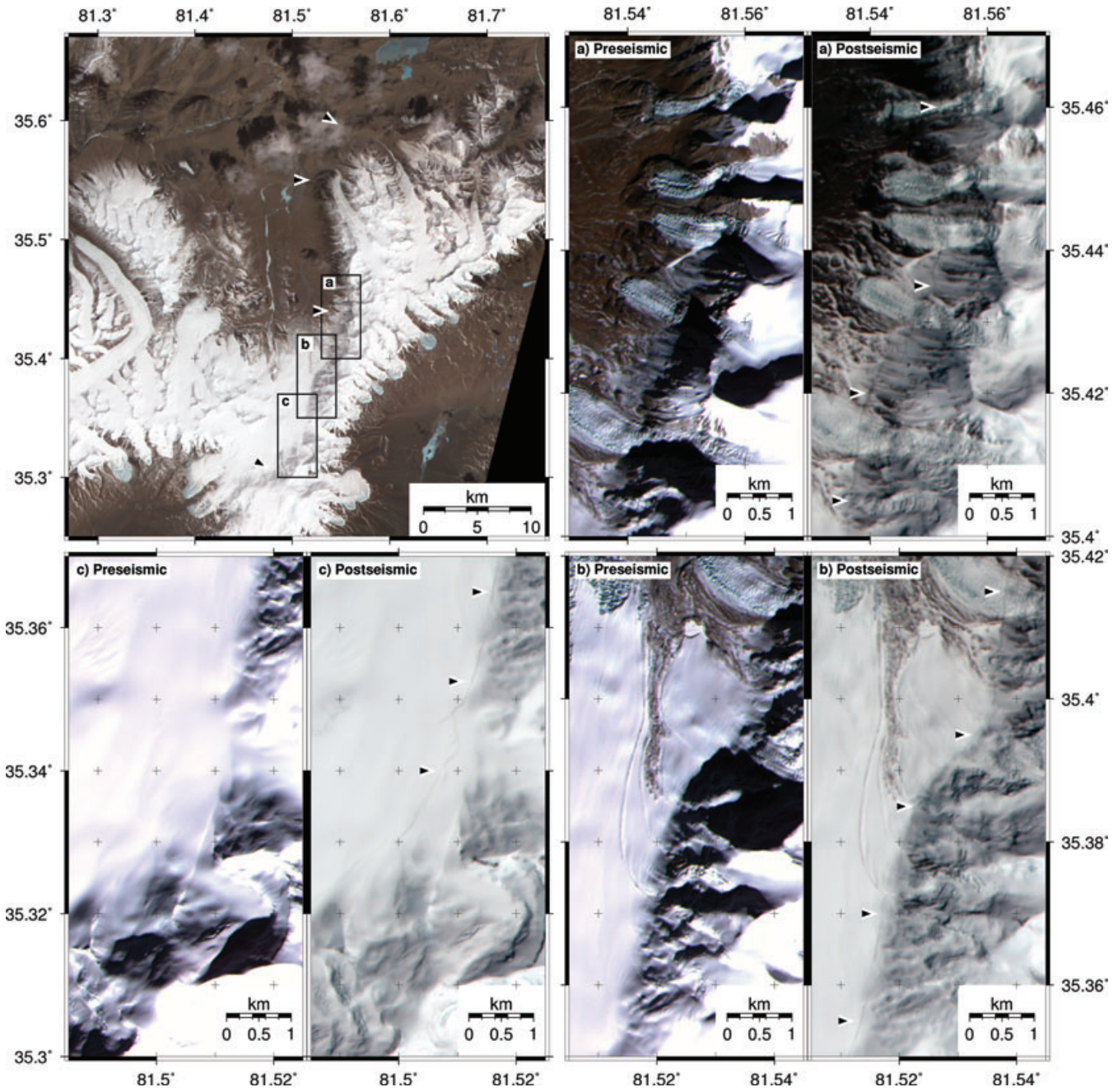

Figure 12. (Top left-hand panel) ASTER satellite image (bands 321, 15 m resolution) of region acquired on the 2008 April 21, one month after the earthquake. The break in topography is seen running almost north–south, beginning in the top-centre of the image and running south for 10 km (marked by black and white arrows). The strike of the scarp then moves around to the SSW and runs for another 15 km. Lettered boxes (a–c) delineate the enlarged regions of the fault, clockwise from top right. A pre-seismic image from the 2007 December 17 is compared with the post-seismic image, in the latter of which surface ruptures are faintly visible (black and white arrows) in the snow cover.

interferograms (Fig. 13). In addition, the top of the rupture is fixed to be at the surface for the middle and southern segments, on the basis of the surface ruptures observed on the ASTER images. We therefore solve for dip, rake, slip and bottom depth on each fault segment, in addition to the top depth for the most northerly segment.

We down-sampled the interferogram data from each track to approximately 1000 points as described previously in Section 2, but in the case of data from tracks 248 and 284 which only cover the western region of deformation, we sample only half as many points (Table 6). Additionally, the data from each track is assigned a relative weight based upon the range of look directions and coverage of data. As there are fewer descending passes than ascending, the former data sets are weighted twice as highly as the latter (Table 6).

The results of the inversion for uniform slip on the three fault segments are given in Table 7. The two main segments (2 and 3) have a similar slip of ∼4 m and dips of 60° and 52° respectively, with a significant component of strike-slip motion for the central segment. Motion on the most northerly segment is relatively minor, with only 1.5 m slip on a moderately dipping (43°), shallow normal fault.

Although the uniform slip modelling produces an overall fit to the data whose mean weighted rms of 11.3 cm is equivalent to

© 2010 The Authors, *GJI*
Geophysical Journal International © 2010 RAS

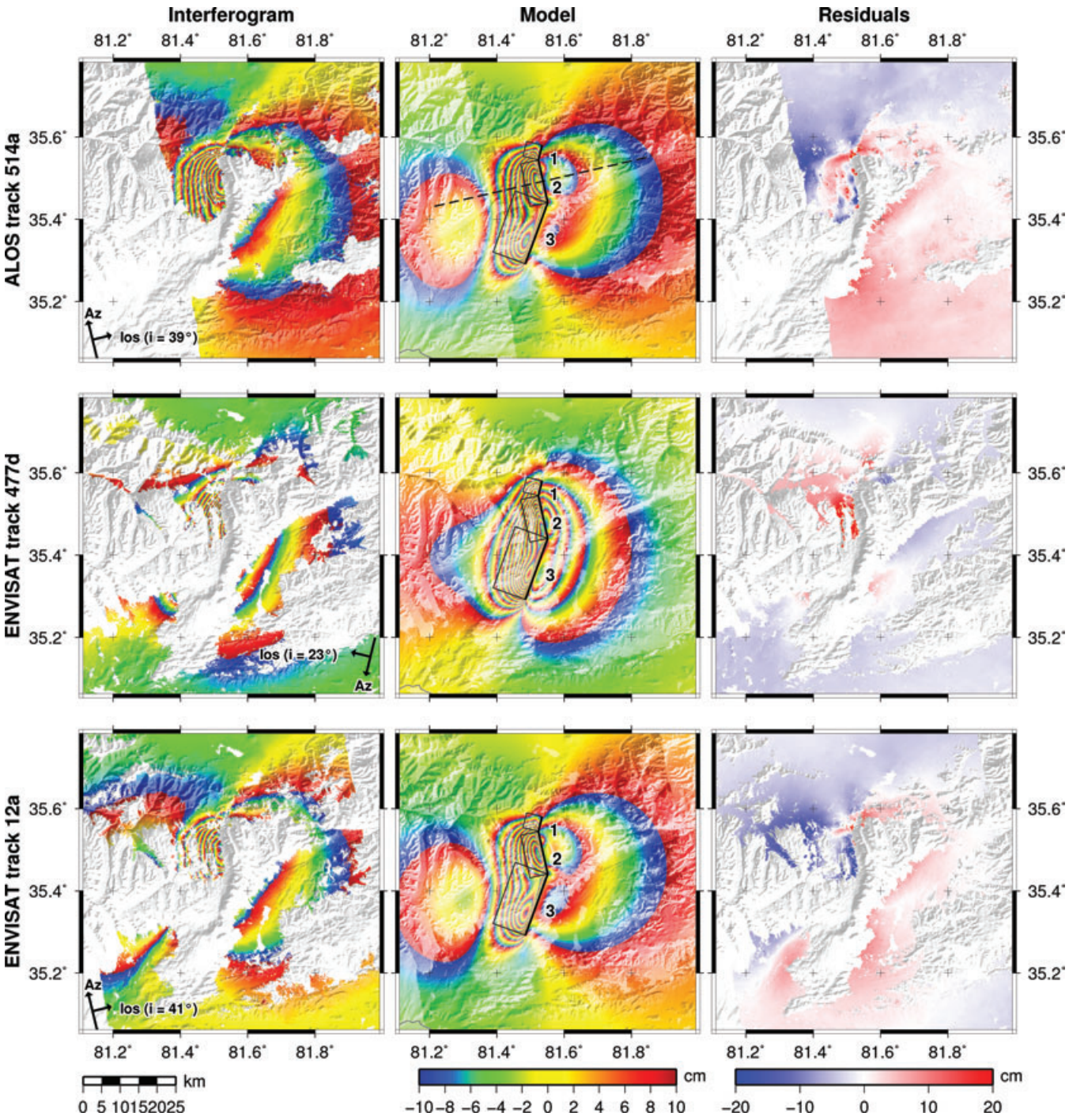

Figure 13. Yutian earthquake interferograms for distributed slip with fixed rake models and residuals. Interferograms for the five other tracks used in the modelling, but not shown here, are given in the on-line supporting information. Symbols as for Fig. 4.

about 5 per cent of the maximum surface displacement, there are significant residuals in the hanging wall of the faults, which vary systematically along strike. In addition, there is unmodelled signal to the southwest of the southern segment, and the descending track 477 has a large weighted residual. Therefore, we also modelled the fault slip on a number of discrete patches to investigate whether we could resolve distributed slip on the fault planes.

The location of each fault was fixed and, using the fault orientation given for uniform slip in Table 7, we extended all segments down dip, and extended the northern and southern fault segments along strike, then subdivided the fault into an array of rectangular 1 km long × 1 km depth elements (Fig. 14). We solved for slip on each element for two cases: a single component (fixed rake) and for two orthogonal components (variable rake). The results for each solution are shown in Table 7. The introduction of variable slip reduces the rms residual to 7.4 cm and reduces the size and extent of the systematic residuals. Allowing the further complexity of variable rake produces only a minor further reduction of the rms to 7.0 cm, with no qualitative change to the pattern of residuals. The interferogram models and residuals for three selected tracks for the

© 2010 The Authors, *GJI*
Geophysical Journal International © 2010 RAS

Table 6. Details of interferograms for the 2008 March 20, M_w 7.1, Yutian earthquake. Caption as for Table 2.

Satellite	Track no.	Direction (asc/dsc)	Incidence (°)	Master (yy/mm/dd)	Slave (yy/mm/dd)	ΔT (dys)	ΔPT (dys)	$B_\perp$ (m)	σ^2 (cm^2)	Distance (km)	Data (km)	Weight	RMS (cm)		
													Uniform	Fix λ	Vary λ
Env	12	asc	41	07/02/27	08/04/22	420	33	21	0.3	8.5	1005	0.8	5.7	5.7	5.0
Env	155	asc	23	08/02/22	08/05/02	70	43	−40	0.4	14.8	1000	0.8	5.1	3.6	3.3
Env	248	dsc	23	07/03/16	08/04/04	385	15	19	0.3	4.8	501	1.6	7.1	4.8	4.5
Env	284	asc	41	07/11/18	08/05/11	175	52	123	0.3	3.9	501	0.8	2.7	2.4	2.2
Env	427	asc	23	06/08/30	08/06/25	665	97	48	1.8	2.7	1000	0.8	4.8	4.2	3.9
Env	477	dsc	23	07/04/01	08/04/20	385	31	92	0.5	7.4	1007	1.6	25.8	16.0	15.3
ALOS	514	asc	39	08/02/24	08/05/26	92	67	41	0.5	5.7	1000	0.8	8.1	5.1	4.6
ALOS	515	asc	39	08/01/26	08/04/27	92	38	−1230	0.4	3.0	1005	0.8	7.0	4.9	4.4

Table 7. Fault plane parameters for the Yutian earthquake. Caption as for Table 3 except for column 2 which denotes the fault segment as shown in Fig. 13 and the body wave source dimension estimate, where the whole seismogenic layer of 15 km is assumed to have ruptured and only a fault length and slip is estimated. Therefore, the length scales as the square root of the moment, $M_0 = (15/\sin(\delta)) \cdot 5 \times 10^{-5}\ \mu L^2$, where δ is the seismologically determined fault dip and μ is the rigidity, equal to 3.2×10^{10} Pa. Total fault length, moment and M_w summed across the segments are shown at the bottom of each model.

Model	no.	Strike (°)	Dip (°)	Rake (°)	Slip (m)	Longitude (°)	Latitude (°)	Length (km)	Top (km)	Bottom (km)	Centroid (km)	Moment, $M_0 \times 10^{18}$ (Nm)	M_w
InSAR-u	1	194	43	268	1.5	81.53	35.56	4.1	0.0	4.0	2	1.1	6.0
		fixed	±0.3	±0.6	±0.01	fixed	fixed	fixed	±0.01	±0.04	±0.02	±0.02	
	2	168	60	295	4.1	81.54	35.49	11.8	0.0	8.4	4.2	15.0	6.7
		fixed	±0.1	±0.3	±0.01	fixed	fixed	fixed	fixed	±0.03	±0.01	±0.04	
	3	200	52	284	3.9	81.52	35.37	17.6	0.0	11.7	5.8	32.9	6.9
		fixed	±0.2	±0.2	±0.02	fixed	fixed	fixed	fixed	±0.05	±0.02	±0.15	
								33.5				49	7.1
InSAR-d-fr	1	194	43	268	0.7	81.53	35.56	8	0	7	3	1.9	6.1
	2	167	60	295	3.6	81.54	35.49	12	0	10	4	19.8	6.8
	3	200	52	284	2.9	81.52	35.37	22	0	12	6	31.2	6.9
								42				52.9	7.1
InSAR-d-vr	1	194	43	261	0.5	81.53	35.56	12	0	10	4	2.7	6.2
	2	167	60	303	3.2	81.54	35.50	12	0	10	4	18.5	6.7
	3	200	52	285	3.0	81.52	35.36	21	0	13	7	33.5	6.9
								45				54.4	7.1
BW		206	45	285	2			40	0	15	6	54.4	7.1
1 fault													
BW	2	165	62	295	0.9			18	0	15	6	8.5	6.5
2 fault	3	206	45	285	1.9			37	0	15	7	46	7.0
								55				54.5	7.1
GCMT		203	52	286		81.37	35.43			12	54	7.1	
USGS		219	69	292		81.47	35.49			10	83	7.2	

fixed rake solution are given in Fig. 13. The slip distribution on which these models are calculated is shown in Fig. 14.

The remaining residuals suggest that there may have been additional displacements that our data are inadequate to constrain. The ALOS data for ascending track 514 has three fringes of residuals indicating 30 cm of unmodelled line-of-sight displacement in the hanging wall of the middle fault segment, as is similar for ascending track 12. Track 12 also shows 10 cm of unmodelled deformation in the south. The distributed-slip models indicate that there is significant slip on the southern end of the southern segment, beyond where the sharp topographic front and surface ruptures were mapped (Fig. 12). It is possible that this slip is located on a fault segment that steps to the west 5–10 km, but it was not possible with the data to constrain this from the relatively small interferometric signal.

The distribution of slip from the calculated model is predominately rectangular in form (Fig. 13). The two main segments show maximum slip of 5 m over a depth range of 2–7 km. Slip of up to 2 m occurs along strike from the southern limit of the uniform model. The minor northern segment indicates up to 2 m slip over a shallow depth range 0–8 km. The model also indicates slip of around 2 m in the top 1 km for the two main segments, and with some slip down to 15 km on the southern segment.

The noise level in the interferograms is small at ∼1 cm (Table 6) in comparison with the maximum deformation signal observed (2 m) from this earthquake, and many of the fault parameters such as strike and location are constrained by other observations and therefore do not trade off with one another. As a result the estimated parameter errors are relatively small (Table 7), the greatest being for the most southern segment, where there is a lack of near-field deformation signals. The calculated error from the Monte Carlo analysis for the distributed slip is predominantly in the 5–10 cm range (Fig. 14), with the maximum centred around the maximum slip on the southern fault where there is an absence of near-field interferometric data.

5.3 Teleseismic body wave modelling

The teleseismic body waveforms were modelled for both a single fault and a two-segment fault. The fault parameters are given in Table 7 and the minimum misfit solutions for *P* and *SH* waves are given in the on-line Appendix C. The single fault solution

© 2010 The Authors, *GJI*
Geophysical Journal International © 2010 RAS

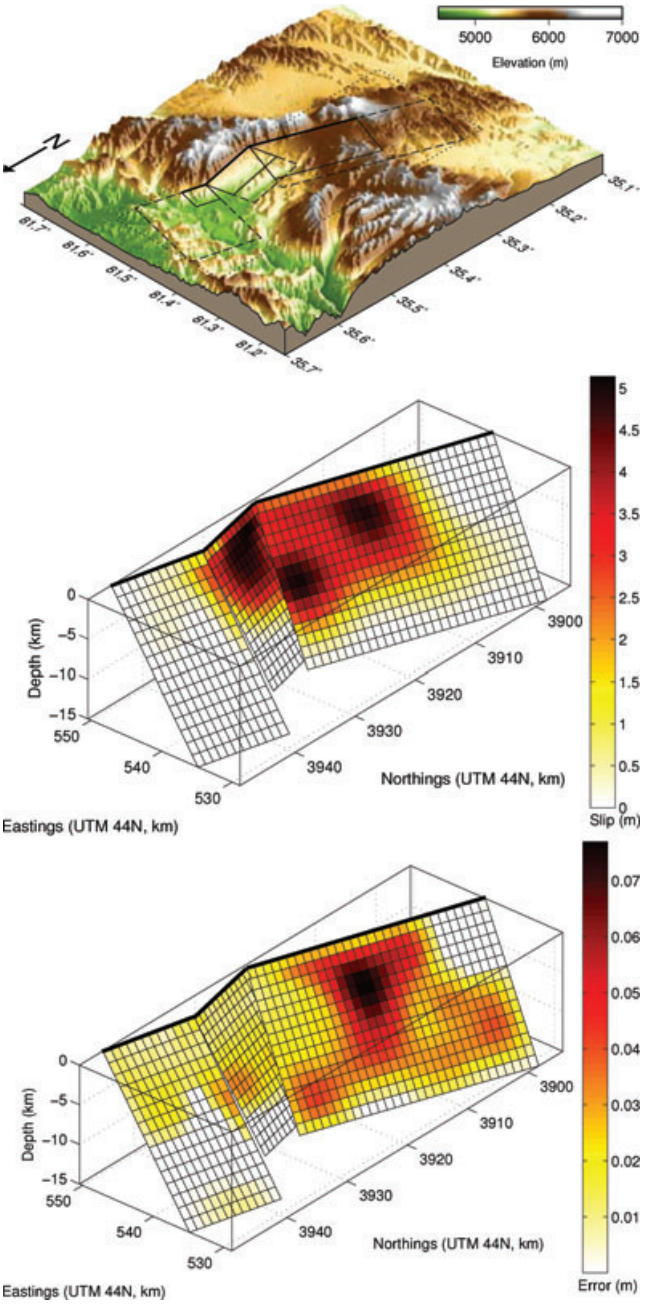

Figure 14. Yutian earthquake slip distribution with a fixed rake based upon the fault orientation from uniform slip modelling. Symbols as for Fig. 9.

yields a SSE striking, 45° dipping fault with a centroid depth of 6 km, with a moderate component of left-lateral sense of slip. For the two-segment solution, the strike, dip and rake are held to those constrained by the InSAR observations for segments 2 and 3 (Table 7) and only the centroid depth and moment are solved for. The two-segment solution yields an similarly well-fitting solution to the seismograms, with centroid depths 6–7 km, a rupture propagation south to north, and with five times the moment release on the southern segment versus the northern. There is close agreement between the InSAR solutions and those from the body wave modelling, and the moment from InSAR slip model with fixed rake matches that calculated from the body wave and GCMT catalogue.

5.4 Summary

The M_w 7.1 Yutian earthquake on the northeastern edge of the Tibetan Plateau principally involved N–S striking, westward dipping, normal faulting with a maximum slip of 5 m and a higher than average slip-to-length ratio of $\sim 13 \times 10^{-5}$. The size of the earthquake means that it is likely to have ruptured the entire seismogenic thickness; body wave modelling places the centroid at ∼7 km and InSAR distributed slip modelling indicates significant slip from the surface down to 15 km.

The earthquake is clearly associated with a strong, linear topographic feature, with the fault cutting through the high elevation, resulting in relief of 2000 m. The fault slip extends at depth to the south and could indicate a southward propagation of extension in the immediate area. The sinistral sense of strike-slip motion on the Yutian normal fault (Table 7) is sympathetic to that of the left-lateral Altyn Tagh strike-slip fault 50 km to the north (Fig. 10). The sense of slip in the Yutian earthquake can be interpreted as arising from an extensional stepover on the Longmu–Gozha Co fault system (Fig. 10). However, this earthquake occurred in the highest region on earth, as measured from topography averaged over a 100 km length-scale. This observation is consistent with the contention (Molnar & Tapponnier 1978) that extension is linked to the high gravitational potential energy of this area.

6 THE 2008 AUGUST ZHONGBA EARTHQUAKE

The 2008 August 25, M_w 6.7 Zhongba earthquake took place in western Xizang region, China (Fig. 1 and 15). The preliminary centroid moment tensor estimate from the USGS indicated a N–S striking normal faulting event with a significant strike-slip component, as did the GCMT solution. Some local damage occurred to buildings in Zhongba county and media reports indicate that the earthquake was felt quite strongly as far south as India. A M_w 6.0 aftershock, with a strike-slip mechanism, took place one month later (Fig. 15). The ratio of magnitudes means the strike-slip event released one-tenth of the moment of the main normal faulting earthquake and therefore it is neglected in the modelling.

The 2008 August event was the most recent of three large normal faulting earthquakes in the past few years in this region. On the 2004 July 11, a westward-dipping M_w 6.2 fault ruptured 30 km to the ESE of the 2008 event, and on the 2005 April 7, a similarly westward-dipping M_w 6.2 normal faulting event occurred a further 20 km south of the earlier event. The details of the models for these earlier events can be found in Appendix A.

The Zhongba earthquake is situated on the Lunggar Rift, which forms part of the pronounced southern Tibetan normal faulting systems (Armijo *et al.* 1986), just north of the Indus Zangbo suture (Fig. 1). The 2004, 2005 and 2008 Zhongba earthquakes indicate extension on a number of faults, both eastward and westward dipping, in the Lunggar Rift. The 2008 earthquake occurred on the most prominent graben in the normal faulting system in a region of relatively higher topography above 5000 m (Fig. 15). Kapp *et al.* (2008) mapped the normal faults in the main part of the Lunggar Rift, 50–100 km north of the events studied here. They inferred that the active normal faults offsetting Quaternary sediments are close to the centre of the rift, within the basin. They mapped inactive normal faults and detachment faults bounding the western edge of the system. (U-Th)-He apatite ages of 0.5–5 Ma on mylonitic leucogranites and orthogneises indicate rapid exhumation in the Pliocene–Pleistocene which Kapp *et al.* (2008) assume occurred

© 2010 The Authors, *GJI*
Geophysical Journal International © 2010 RAS

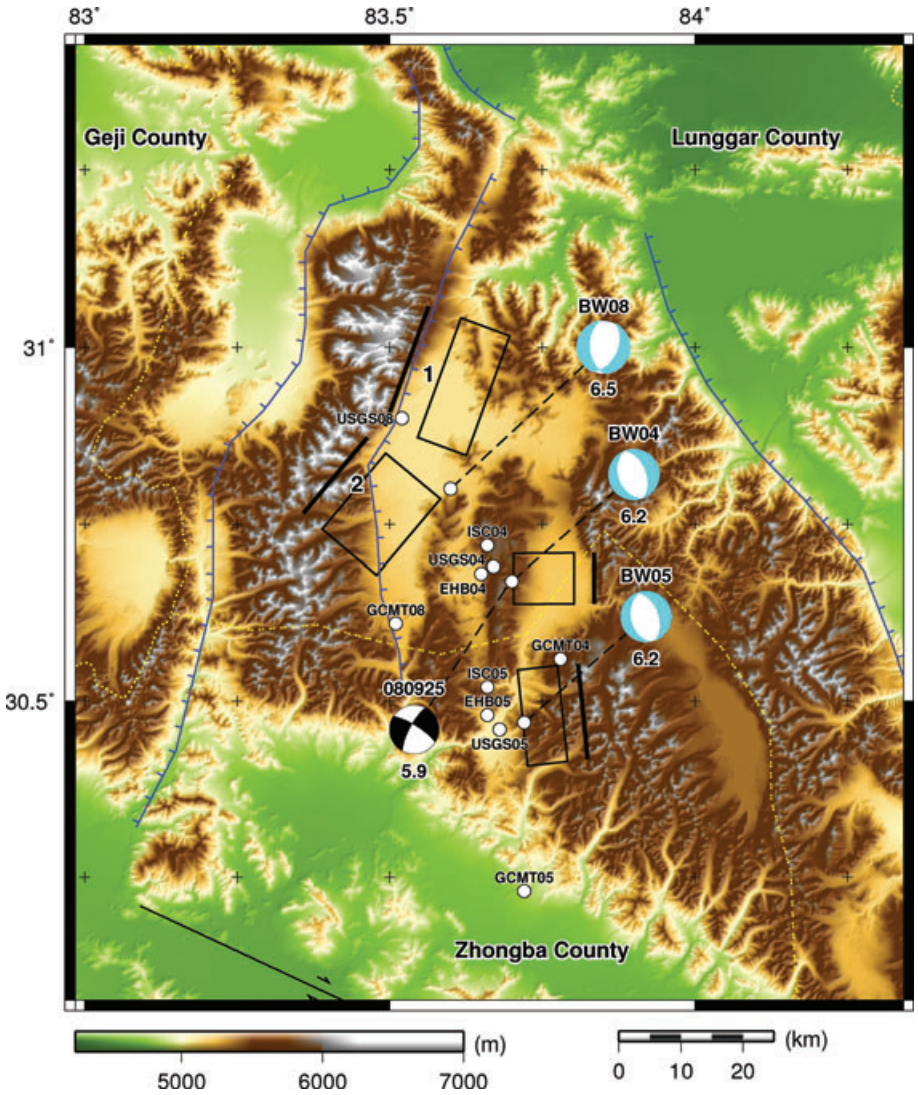

Figure 15. Shaded relief elevation map of the Zhongba region, central Tibet for the three normal faulting events that occurred in 2008, 2005 and 2004. Caption as for Fig. 3.

on what they refer to as now inactive detachment faults bounding the western edge of the rift.

6.1 Fault geometry estimated from InSAR

Four ENVISAT interferograms have suitable acquisitions spanning the 2008 earthquake (Table 8), with two passes each on both descending and ascending inclinations. The coherence is good for tracks 241a and 119d, but the more mountainous regions of the footwall are incoherent in the other two tracks. The most northerly lobe of deformation has its maximum signal masked by the presence of a lake, most likely colocated with the greatest rate of subsidence in the graben.

A major north–south trending graben structure is visible in the topography (Fig. 15), with peaks in the western footwall above 6 km, and a relatively flat hanging wall at around 5 km elevation. The most northern lobe of deformation seen in the interferometry is clearly associated with this mountain front (Fig. 16, left-hand column), with the mountain range striking NNE. This topographic feature runs for 60 km, before striking to the south and continuing for a further 40 km. However, the deformation pattern seen in the interferometry

Table 8. Details of interferograms for the Zhongba M_w 6.7 earthquake 2008 August 25. Caption as for Table 2.

Satellite	Track no.	Direction (asc/dsc)	Incidence (°)	Master (yy/mm/dd)	Slave (yy/mm/dd)	ΔT (dys)	ΔPT (dys)	$B_\perp$ (m)	σ^2 (cm^2)	Distance (km)	Data (pts)	Weight	RMS (cm)		
													Uniform	Fix λ	Vary λ
Env	119	dsc	23	08/04/30	08/09/17	140	23	247	0.21	4.7	1005	1	2.5	1.7	1.5
Env	241	asc	41	08/08/21	08/10/30	70	66	235	0.53	5.7	1007	1	2.4	1.9	1.8
Env	384	asc	23	06/08/27	08/10/05	770	41	407	0.84	7.6	1003	1	2.2	1.7	1.7
Env	391	dsc	23	07/04/30	08/09/01	490	7	67	0.22	4.4	1003	1	2.2	1.1	0.9

© 2010 The Authors, *GJI*
Geophysical Journal International © 2010 RAS

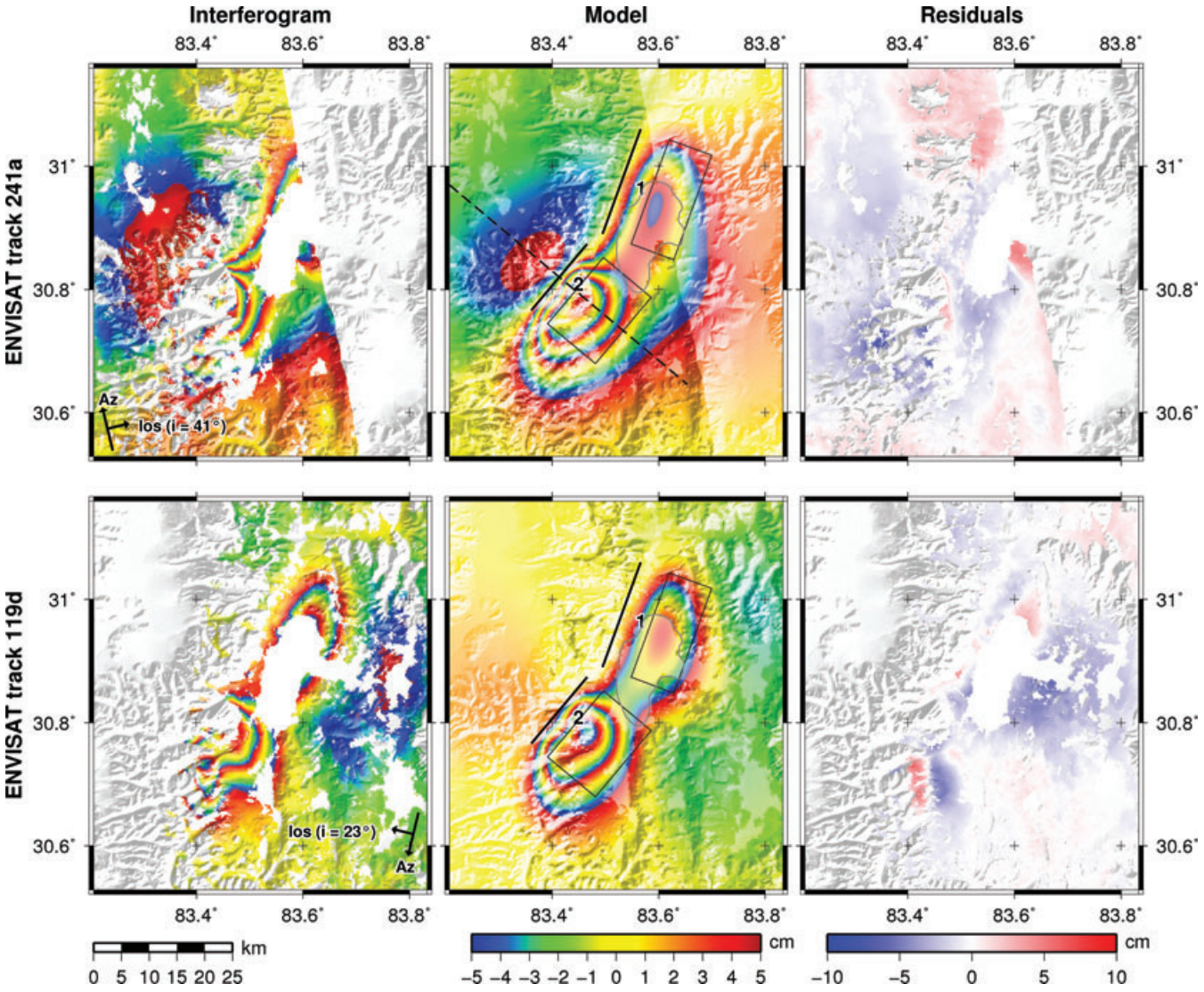

Figure 16. Zhongba earthquake interferograms for distributed slip modelling with a fixed rake. Interferograms for the two other tracks used in the modelling, but not shown here, are given in the on-line supporting information. Details as for Fig. 4.

indicates a trend in the ground displacements more to the SW at a high angle to this front. Closer examination of the topography does indeed indicate a change in strike of this topographic front to the SW. Therefore, we choose to model the earthquake as having occurred on two separate fault segments, with strikes and locations fixed to that observed in the topography (Table 9). We invert for the remaining fault parameters as described in previous sections. Initial inversions resulted in the length of the segments strongly trading off against each other. Therefore we fixed the length of the northern segment from the topography and interferogram fringe pattern to 20 km, whilst allowing the southern one to vary.

The uniform slip solution for the two segments yields near identical dips of ∼42° and rakes of ∼308° indicating a large component of left-lateral slip (Table 9), with 0.9 m slip on the southern segment and 0.6 m on the northern segment. The inversions indicate that both segments are buried, rectangular faults with slip from 3 km below the surface down to 13 km. Formal errors from a Monte Carlo analysis for each of the free fault parameters are given in Table 9. Dip and rake each vary by 1–2°, slip by 2–8 per cent, fault dimensions by 0.1–0.3 km and moment by $\sim 1 \times 10^{17}$ N m.

The range of rms misfit between the interferograms and models calculated from the uniform slip parameters is of the order 2.4 cm for each track or 10 per cent of the maximum surface displacement (Table 8). Some residual fringes are observed after subtracting the uniform model from the observed interferogram data for the southern segment, where a double maximum in line-of-sight displacement is observed.

In attempt to further refine the uniform slip model for the Zhongba 2008 earthquake, we inverted the interferogram data for slip on 1 km patches as described in previous sections. The two fault segments are extended along strike, with the southern segment continuing up to the point of surface intersection with the northern segment (Fig. 17). The fault dips and rakes are fixed at those for the uniform model.

Allowing variable slip improved the rms fit to the interferograms (Table 8) and reduces the sizes of systematic residuals associated with the southern termination of the southern fault segment (Fig. 16). The distribution of slip with depth (Fig. 17) indicates a buried fault for the northern segment with slip between depths of 3 and 20 km. The southern segment has significant slip much

© 2010 The Authors, *GJI*
Geophysical Journal International © 2010 RAS

Table 9. Zhongba fault plane parameters from inverting interferometric data, from *P* and *SH* body wave modelling for a single and two segment fault, and as listed in the Global CMT and USGS catalogues. Details as for Table 5.

Model	no.	Strike (°)	Dip (°)	Rake (°)	Slip (m)	Longitude (°)	Latitude (°)	Length (km)	Top (km)	Bottom (km)	Centroid (km)	Moment, $M_0 \times 10^{18}$ (Nm)	M_w
InSAR-u	1	020	43	309	0.6	83.53	30.97	20	5.1	12.7	8.9	4.5	6.4
		Fixed	±2	±2	±0.05	Fixed	Fixed	Fixed	±0.3	±0.3	±0.2	±0.1	
	2	040	42	307	0.9	83.41	30.82	15.6	3.4	13.4	8.4	6.9	6.5
		Fixed	±1	±1	±0.02	Fixed	Fixed	±0.2	±0.1	±0.2	±0.1	±0.1	
								35.6				11.4	6.6
InSAR-d-fr	1	020	43	309	0.27	83.53	30.97	30	4	15	9	5.3	6.4
	2	040	42	307	0.59	83.41	30.82	24	1	16	9	7.2	6.5
								54				12.5	6.7
InSAR-d-vr	1	020	43	302	0.32	83.53	30.97	30	3	20	10	7.1	6.5
	2	040	42	283	0.48	83.41	30.82	28	1	17	8	8.4	6.5
								58				15.5	6.7
Body wave		025	46	292	0.90			18	2	14	8	9.4	6.5
Body wave	1	020	43	309	0.75			15	3	13	8	5.2	6.4
	2	040	42	307	0.65			13	4	12	8	3.2	6.2
								29				8.4	6.5
GCMT		030	48	312		83.51	30.61			17.3	13.9	6.7	
USGS		006	29	276		83.52	30.90			12	12	6.6	

closer to the surface, and possibly could have ruptured the surface for a few kilometres. Maximum slip was greatest on the southern fault at about 1.2 m, about one-and-a-half times that in the north. A shallower southern-most extent is resolvable for the southern fault as inferred by the pattern of surface displacements in the InSAR (Fig. 16). A solution allowing variable rake did not produce a significant reduction in residuals. The standard deviation in calculated slip from a Monte Carlo analysis is greatest for the northern segment at up to 3 cm (Fig. 17).

6.2 Teleseismic body wave modelling

The body waves from this event were modelled for both a single fault and for two segments. The fault parameters are given in Table 9 and the minimum misfit solutions for *P* and *SH* waves are given in the on-line Appendix C. The single fault solution yields a NNE striking, 46° dipping fault with a centroid depth of 8 km, and a moderate component of left-lateral slip. For the two-segment solution, the strike, dip and rake are held to those constrained by the InSAR observations and only the centroid depth and moment are solved for. The two-segment solution yields an similarly well-fitting solution to the seismograms, with centroid depths maintained at 8 km, the northern segment rupturing before the southern, and a moment release 1.6 times greater on the northern segment.

There is close agreement between the InSAR solutions and those from the body wave modelling for the fault parameters, but the body wave solution has a total moment significantly below (∼25 per cent) those estimated from InSAR and the catalogued seismological solutions. Additionally, for the two fault segment model, the body wave solutions estimate more moment release on the northern rather than southern segment which is the reverse of the InSAR solutions.

6.3 Summary

The 2008 August M_w 6.7 Zhongba county normal faulting earthquake occurred on two fault segments, dipping eastward at 43° and with a large component of left-lateral slip. The northern fault segment is clearly associated with a topographic front, whereas the surface projection of the southern segment cuts into the high topography of the region.

The active faulting measured here is located on the edge of the normal faulting system, bounding the high topography. This is in contrast to the active normal faults mapped on the part of the fault system 50–100 km northwards (Kapp *et al.* 2008), which are positioned in the centre of the rift. Elastic dislocation modelling of InSAR displacements indicates slip approaches the surface; InSAR and body wave solutions both yield a centroid depth of 8–9 km, and the InSAR suggests that rupture extended to a depth of about 13 km. This earthquake is the third in a sequence of normal faulting earthquakes closely spaced in time and location, that indicates continued dissection of high topography and east–west extension. All of these earthquakes took place on faults dipping between 40° and 50°, with slip vectors orientated ENW–WSW (Fig. 15 and Table A2).

7 DISCUSSION

The five normal faulting events that occurred on the Tibetan Plateau in 2008, along with three recent related events (see Appendices), provide an opportunity to re-examine the role of north–south striking normal faulting in accommodating extension of the plateau. The demonstration that crustal thinning observed in normal faulting earthquakes over the past ∼50 yr is compatible with the average thinning rate for the plateau estimated geodetically (Section 7.1.1), and the fact that the earthquakes investigated here represent almost two-thirds of the normal faulting moment release on the plateau in that interval (Fig. 2), encourage us to use our observations to make general remarks about the normal faulting on the plateau.

7.1 Crustal deformation in Tibet

7.1.1 Rates of crustal thinning

The active tectonics of Tibet is dominated by strike-slip faulting, with minor normal faulting; the *T*-axes of the earthquakes for which reliable focal mechanisms can be obtained are aligned approximately E20°S (Fig. 18), suggesting that the plateau is accommodating distributed extension in this direction, and shortening along N20°E (e.g. Molnar & Qidong 1984; Molnar & Lyon-Caen 1989). The relatively sparse GPS data on the plateau are consistent with this

© 2010 The Authors, *GJI*
Geophysical Journal International © 2010 RAS

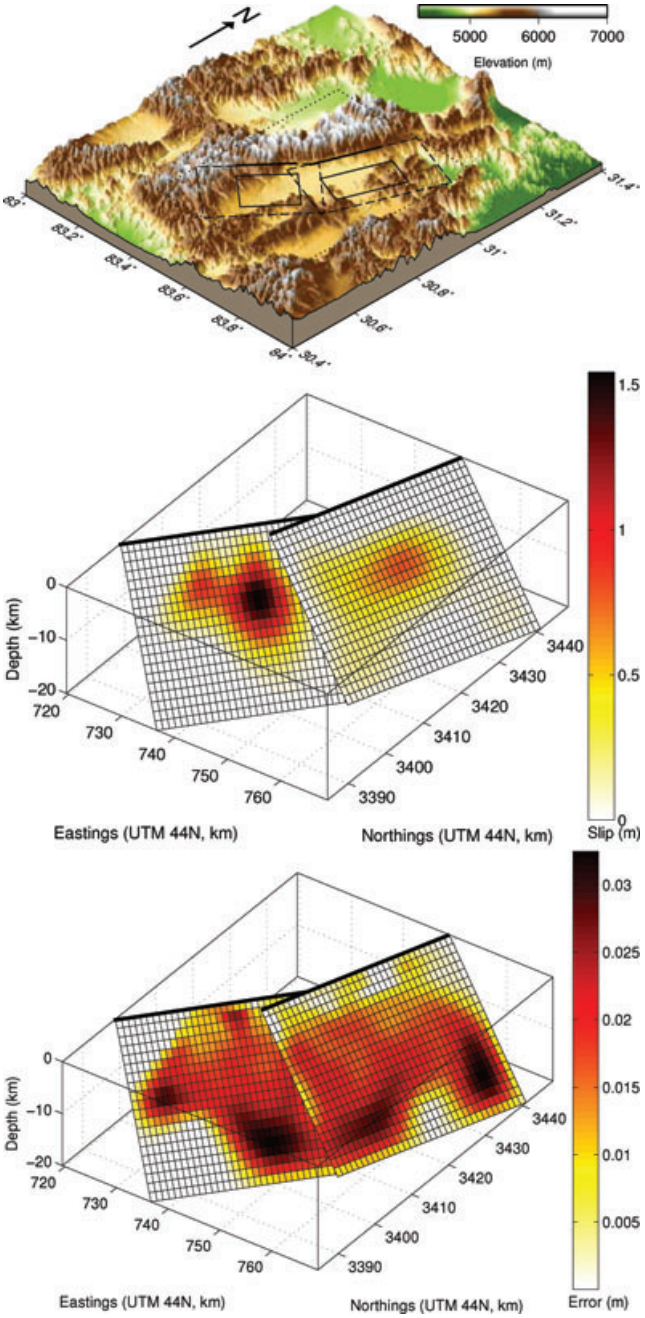

Figure 17. Zhongba earthquake slip distribution with fixed rake based upon the fault orientation from uniform slip modelling. Symbols as for Figure 9.

picture, suggesting extensional strain of $2.1 \pm 0.3 \times 10^{-8}$ per year in the direction of E20°S, and contraction in the N20°E direction at $-1.6 \pm 0.4 \times 10^{-8}$ per year (Zhang *et al.* 2004).

In order to relate geodetic strain rate to finite strain expressed in faults, we interpret the sum of the two horizontal principal strain rates as being equal to the negative vertical strain rate (i.e. we assume no volumetric strain in the long term). The differences between the rate of extension in the E20°S direction and of contraction in the orthogonal direction reflects vertical strain and crustal thinning (there is no evidence for crustal thickening in the active tectonics of the interior of the plateau: Armijo *et al.* 1989; Molnar & Lyon-Caen 1989; Taylor *et al.* 2003). However, uncertainties in the geodetic data and incompleteness of the seismic record, which is dominated by strike-slip faulting, make it difficult to form a reliable estimate of the rate of crustal thinning.

The GPS geodetic data suggest an average vertical strain rate for the plateau of $-5 \times 10^{-9}\,\mathrm{yr}^{-1}$, though with a formal uncertainty that permits crustal thickening. The total moment release in normal faulting over the past 43 yr (Fig. 2) is 1.4×10^{20} N m, which may be converted to thinning strain rate, using the method of Kostrov (1974):

$$\dot{\varepsilon}_{ij} = \frac{1}{2\mu V t} \sum_n M_{ij}^n, \tag{2}$$

where $\dot{\varepsilon}_{ij}$ is the ij th component of the strain-rate tensor, and $\sum_n M_{ij}^n$ is the sum of the equivalent components of the moment tensors of n earthquakes in a volume V occurring over a time interval t in a medium of shear modulus μ.

Initially, we consider $\dot{\varepsilon}_{zz}$, which is the component of the strain-rate tensor representing linear strain in the vertical direction; without significant error, we treat each earthquake as pure dip-slip and equate $\dot{\varepsilon}_{zz}$ to the scalar moment of the earthquake. We take V for the Tibetan plateau to be the surface area of ground above 4200 m (2×10^6 km^2) multiplied by the thickness of the seismogenic layer, which we estimate to be 15 km, based on the depths of faulting determined here, and from seismic studies (Molnar & Chen 1983; Molnar & Lyon-Caen 1989). With $\mu = 3.23 \times 10^{10}$ Pa, we obtain an estimate of $1.7 \times 10^{-9}\,\mathrm{yr}^{-1}$ for the thinning strain rate (or 2.6×10^{-9} if the seismogenic thickness is assumed to be 10 km (Funning *et al.* 2007), which is consistent with the geodetic data. [Due to the large range in moment between the smallest and largest earthquakes included in this calculation, our estimate increases slightly (by ∼15 per cent) if the contribution from earthquakes smaller than M_w 5.5 is included (Scholz & Cowie 1990).]

7.1.2 Rates of east–west extension

We next attempt to estimate the contribution that the normal faulting makes to the east–west extension in the northern and southern plateau. Several estimates have been made for the rate of extension across the grabens of southern Tibet, both from observations of faulting and from geodesy. Armijo *et al.* (1986) estimated a rate of $10 \pm 5.6\,\mathrm{mm\,yr}^{-1}$ extension in southern Tibet by taking the offset across the Yadong-Gulu graben as representative of grabens in southern Tibet and summing across all grabens; this estimate is consistent with the inference from the distribution of normal- and strike-slip-faulting earthquakes in that at least one half of the ∼15–20 $\mathrm{mm\,yr}^{-1}$ of NNW–SSE extension in southern Tibet is associated with strike-slip faulting (Molnar & Lyon-Caen 1989). The north–south grabens of central and northern Tibet have received less attention than those in the south, but Molnar & Lyon-Caen (1989) concluded from their compilation of pre-1989 earthquakes in Tibet that extension of up to 5 $\mathrm{mm\,yr}^{-1}$ occurs across the grabens of the central and northern parts of the plateau, a conclusion that is supported by field mapping of normal faulting structures in northern Tibet suggesting that rates of extension there are comparable to those in southern Tibet (Yin *et al.* 1999).

Although the Tibetan earthquakes available for study in 1989 had only about half the accumulated moment release of those that have occurred in the region since, the enlarged data set supports the inference of Molnar & Lyon-Caen (1989) that crustal thinning by normal faulting is as important in northern Tibet as in the south. We subdivided the plateau into 10 rectangles, five in southern Tibet, and

© 2010 The Authors, *GJI*
Geophysical Journal International © 2010 RAS

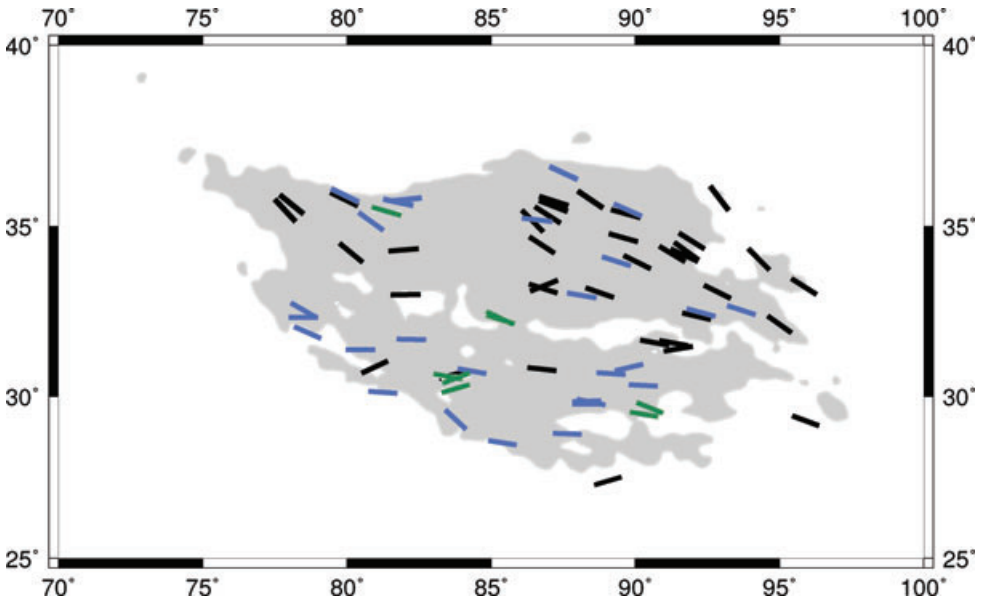

Figure 18. *T* axes of normal faulting (blue) and strike-slip-faulting (black) M_w 5.5+ earthquakes from the Global CMT catalogue 1976–2008 and from Molnar & Lyon-Caen (1989) 1966–1975 with depths shallower than 70 km and occurring in crust with surface elevations above 3500 m. *T*-axes from earthquakes in this study are denoted in green. The grey shaded region denotes the area above 4750 m.

five in the north, and used Kostrov's method (eq. 2) to calculate rates of strain and extension across the region (Fig. 19). In the south, the rate of extension between 76°E and 96°E is just under 3 mm yr^{-1} and for the north it is just under 4 mm yr^{-1}, a large contribution (48 per cent) of which has come from the M_w 7.1 Yutian earthquake studied here. Given the largest earthquake tends to dominate the estimate of total moment in each boxed region due to the short seismic record (Fig. 2), our estimate of extension rate is therefore very sensitive to the recurrence time of these large earthquakes.

7.1.3 Moment release and gravitational potential energy

It has been known for some time that normal faults and normal faulting earthquakes in Tibet are generally confined to altitudes above about 4500 m (Molnar & Lyon-Caen 1989; Molnar *et al.* 1993). All the earthquakes studied here conform to this pattern, taking place without exception in regions whose regionally averaged surface height exceeds 4500 m (Fig. 20). We combine our observations with the catalogue of Molnar & Lyon-Caen (1989), and with the GCMT catalogue of M_w 5.5+ earthquakes, to refine the picture of moment release versus surface height.

We find that significant moment release in normal faulting earthquakes is confined to regions above 4750 m (Fig. 20); this elevation is significantly higher than the ∼4 km estimated by Molnar *et al.* (1993) as the threshold for normal faulting. Indeed most of the moment release occurs above 5 km (Fig. 20). This concentration of moment release is not the result of bias in the distribution of elevation: only about 25 per cent of the area of the plateau lies above 5 km, whereas about 85 per cent of the normal faulting moment release takes place beneath ground higher than this elevation.

Conversely, thrust faulting is confined to the edge of the plateau at low elevations at the Himalayan front, and intermediate elevations in the Qaidam basin in the northeast, and Sichuan basin in the east. The orientations of strike-slip and normal faulting are consistent with east–west crustal extension, whilst thrust faulting at lower elevations continues to thicken the crust and elevate the surface at the plateau margins. This clear relationship between style of deformation and the surface elevation reinforces the suggestions of many authors that contrasts in gravitational potential energy within the continental lithosphere play an important role in the tectonics of the region (e.g. Molnar & Tapponnier 1978; Houseman & England 1986; England & Houseman 1989; Molnar *et al.* 1993).

7.2 Seismological considerations

7.2.1 Earthquake mislocations

The sparsity of seismological stations reporting to the international seismological bulletins in this part of Asia, and the crustal heterogeneity of the Tibetan Plateau and surrounding regions, result in the mislocation of earthquakes in these catalogues due to unmodelled bias in the seismic wave paths. The use of InSAR observations permits the accurate positioning for moderately sized (M5.5+) and relatively shallow (<20 km) events. In most such cases, it is also possible to resolve the ambiguity of the fault slip plane and to determine the fault parameters describing it.

The InSAR-determined locations of the earthquakes we study here are compared, in Fig. 21, with those reported in the GCMT and USGS NEIC catalogues and, for pre-2006 events, with locations reported in the ISC and EHB (Engdahl *et al.* 1998) catalogues. The InSAR location is taken as the surface position immediately above the bottom-centre of the fault in the uniform slip models. This is in order to match the nucleation points of the rupture as measured by the epicentre locations from the short-period seismology, assuming that earthquakes nucleate near the bottom and rupture up, although this introduces some uncertainty if the rupture initiates at one end of the fault. For the earthquakes that occurred on multiple segments (Yutian M_w 7.1 2008 and Zhongba M_w 6.7 2008 events), the average location of the uniform slip model is used, and the comparison is more difficult due to the size of the earthquake (rupture lengths ∼35 km). The results show a systematic bias in the reported locations of the events in the GCMT catalogue of 15–30 km SSE

© 2010 The Authors, *GJI*
Geophysical Journal International © 2010 RAS

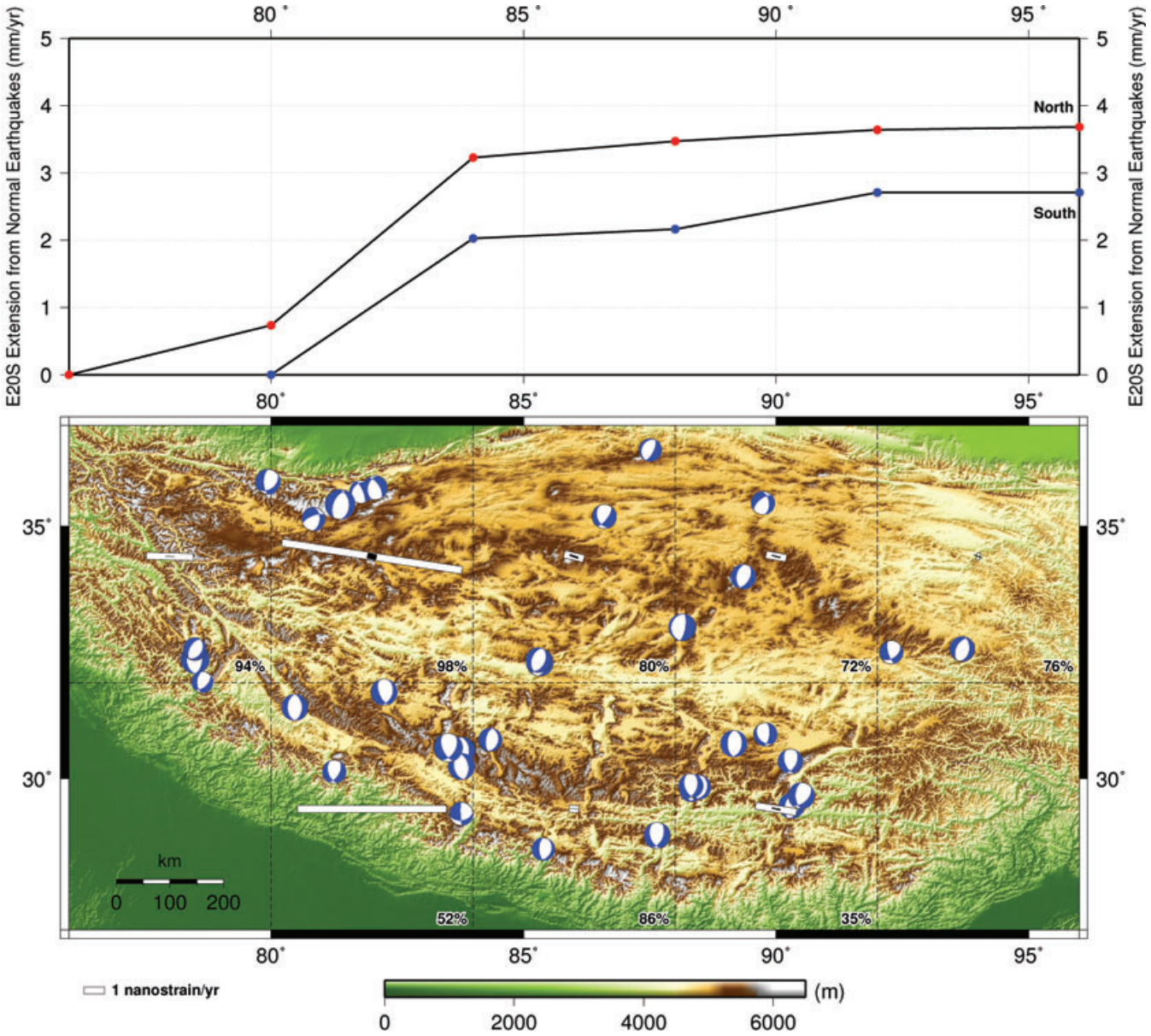

Figure 19. Distribution of M_w 5.5+ normal faulting crustal earthquakes from the Global CMT catalogue 1976–2008 and the compilation of Molnar & Lyon-Caen (1989). Dashed boxes delineate areas in which strain rates were calculated from the summed moment tensors of earthquakes, using the method of Kostrov (eq. 2). White bars show the orientation and magnitude of the principal horizontal extensional strain rate in each box. Numbers in the lower-right hand corner of each box indicate the percentage contribution to the total moment in that region from the largest earthquake. The top figure shows the cumulative extension in the direction E20°S in 4° × 5° bins, for north and south Tibet as defined by the 32° line of latitude.

from the InSAR location in seven out of the eight cases (Fig. 21). The location of the Yutian M_w 7.1 earthquake is more accurate, probably due to the larger number of seismic stations reporting an earthquake of that size. The mislocations from the USGS NEIC catalogue show less bias and mislocation, generally falling more westward or to the south by 5–20 km. There are ISC and EHB locations only for the three earlier earthquakes 1992, 2004 and 2005, and these show a much closer agreement with the InSAR location, and are also similar to the USGS NEIC epicentre.

7.2.2 Moment release comparisons

The moment release calculated from the InSAR uniform and distributed slip (with fixed rake) models are compared with those calculated from seismology (Fig. 22). The same shear modulus was used for the InSAR modelling and body wave analysis to permit direct comparison. It has previously been suggested that geodetically derived seismic moments might be larger than those derived seismically (Feigl *et al.* 1995; Wright *et al.* 1999).

The moments of the InSAR models have a slight systematic positive bias (of significantly less than a factor of two in most cases) with respect to the body wave solution, and generally increase when the InSAR model complexity is increased from uniform to distributed slip (Fig. 22). This positive bias could reflect the inclusion of aseismic slip or postseismic deformation such as afterslip in the InSAR models, as the second satellite pass required to form the interferograms necessarily occurs sometime after the earthquake due to the orbit repeat time of 35–46 d (see supplementary material for

© 2010 The Authors, *GJI*
Geophysical Journal International © 2010 RAS

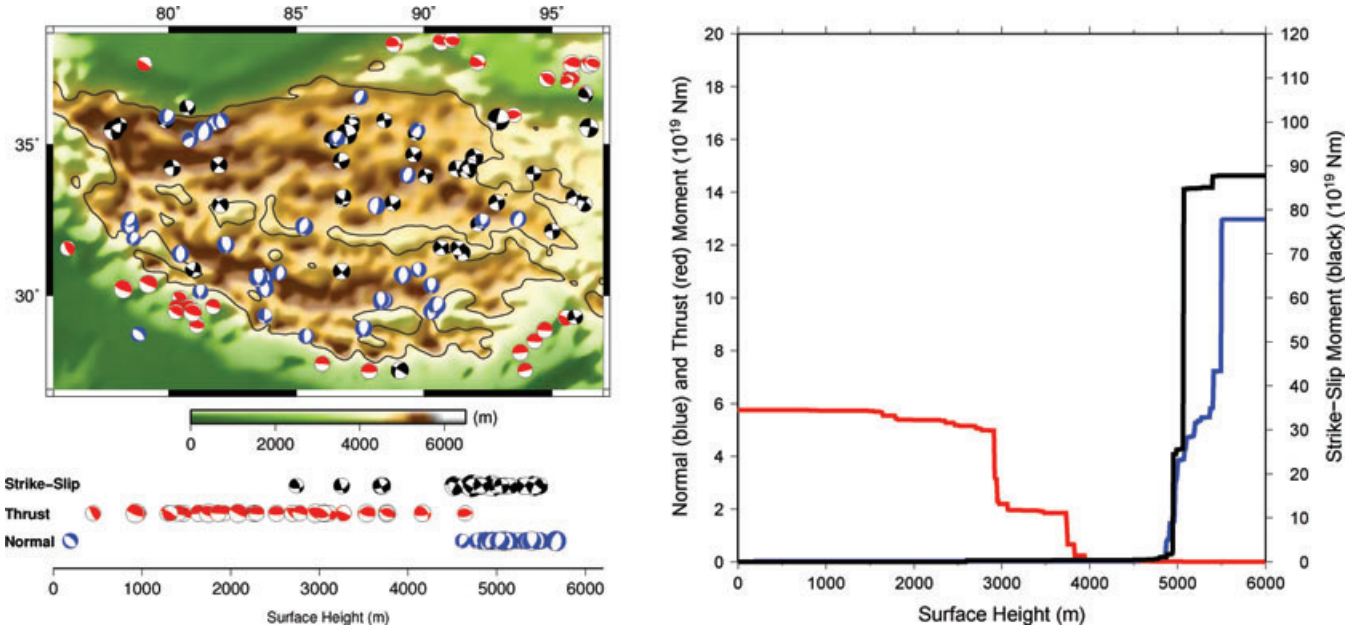

Figure 20. Left-hand panel: earthquake mechanism versus surface height (bottom) from the GCMT catalogue, 1976–2008, and from Molnar & Lyon-Caen (1989), 1966–1975, for M_w 5.5+ and shallow (<70 km) events within the region indicated by the map (top). Topography is Gaussian filtered with a 100 km width and the 4750 m contour is denoted by a black line. Normal faulting events in the area are restricted to 4.5 km and above. Strike-slip faults are above 2.5 km. Thrusting mechanisms bound the plateau edge and are found at most elevations below 4.5 km, particularly clustering below 2 km. The Yutian earthquake on the northwestern edge of the plateau is in the region with the highest long-wavelength elevation for the entire globe, at nearly 6 km. Right-hand panel: cumulative seismic moment release (Nm) from the earthquakes in the same region shown on the left versus filtered surface height. Red line represents moment release (left-hand scale) in thrust-faulting earthquakes, with accumulation going from high to low ground. Accumulation of moment for normal faulting earthquakes (blue line, left-hand scale) and strike-slip earthquakes (black line, right-hand scale) is from low to high ground. Note that the scale for strike-slip moment is six times that for the normal faulting, and therefore a large proportion of the extension rate is likely to be accommodated by strike-slip faulting.

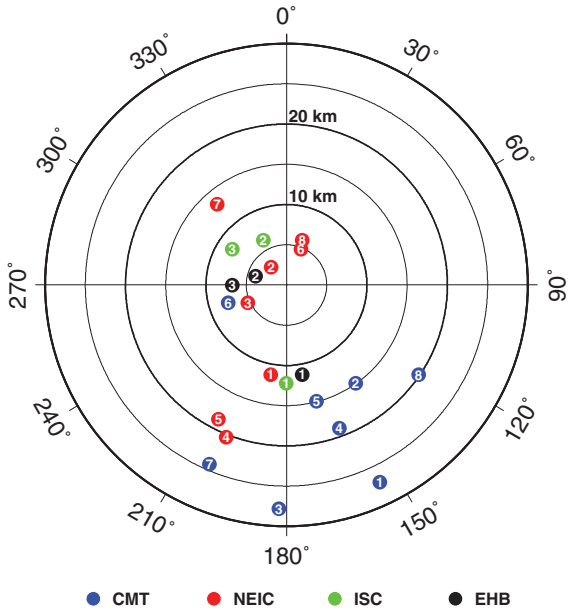

Figure 21. Mislocations of earthquakes by GCMT (blue circles), NEIC USGS PDE (red), ISC (green) and EHB (black) catalogues in azimuth and range relative to that from InSAR determined surface projection of the fault bottom-centre location. Circles are numbered to denote earthquake in date ascending order as listed in Table 1. GCMT derived locations are biased ~15–30 km to the SSE. NEIC PDE locations are not as systematically biased, with only a slight trend in bias to the WSW. There are currently not enough ISC and EHB locations to infer any trends in mislocation, although they give more accurately located positions in the few examples present.

figures of SAR time coverage of each event). Additionally, the interferograms contain atmospheric noise that could also increase the moment, particularly in the distributed-slip models.

There is larger variation between the body wave and USGS/GCMT moments (Fig. 22) with some estimates from the catalogues being almost twice those from our body wave analysis. Possible explanations for the moment discrepancy are that the GCMT looks at more of the wave train energy than the body wave analysis and therefore has higher moment. Alternatively, given that the GCMT solution has difficulty in resolving the M_{xz} and M_{yz} components for shallow events, a shallow dip leads to a trade-off with increased moment (Dziewonski & Woodhouse 1983). However, no systematic underestimation of fault dips from the GCMT catalogue can be seen for these events. Finally, the body wave estimates give very consistent, shallow earthquake depths which match well those from the InSAR modelling. However, the USGS/GCMT solutions tend to give larger depths [or are fixed to a 10 km minimum for the case of GCMT (Dziewonski *et al.* 1981)]. A moment-depth trade-off in the GCMT solution possibly results in the increased moment due to the erroneously deep centroid depth in every case, as was observed to happen for the normal faulting event which occurred in Dinar, Turkey in 1995 (Wright *et al.* 1999).

7.3 The geometry and morphology of normal faulting

7.3.1 The dips of normal faults

The question as to whether normal faults are seismically active at low-angle dips ($\delta < 30°$) in the upper continental crust and their connection with mapped low-angle detachment faults is still very much debated (Axen 2007). Dip estimates for 25 intracontinental

© 2010 The Authors, *GJI*
Geophysical Journal International © 2010 RAS

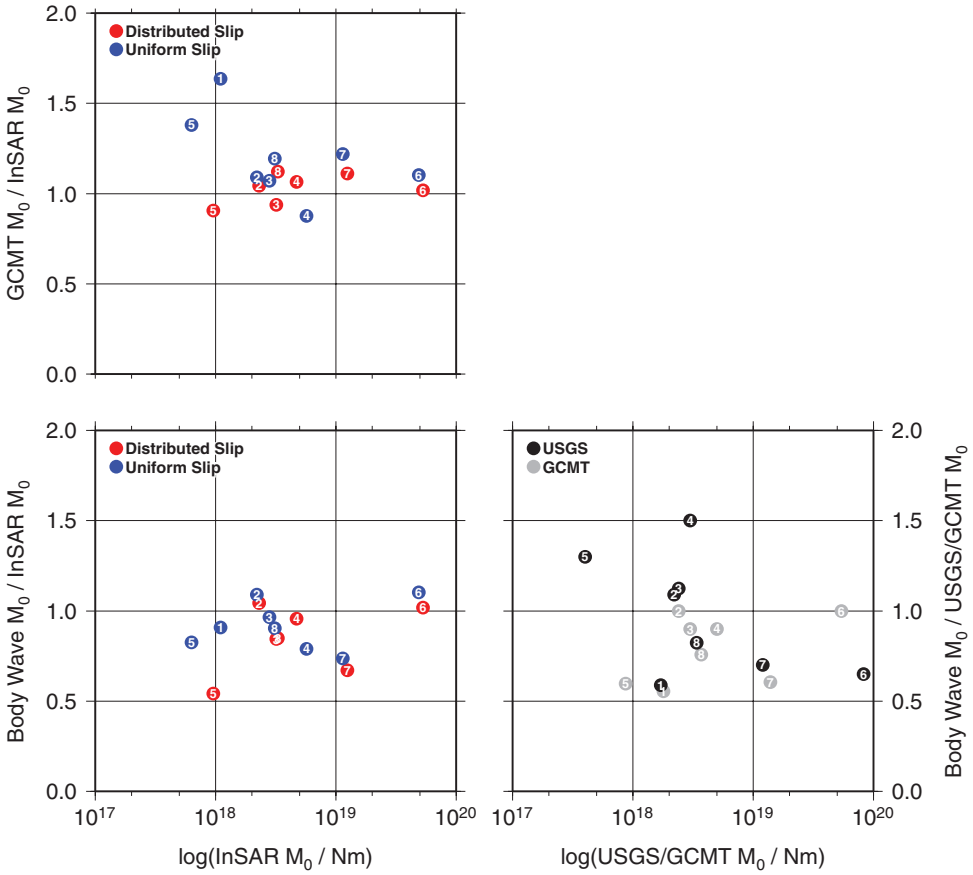

Figure 22. Comparisons of calculated moment release between InSAR models and seismological solutions from the body wave analysis (bottom left-hand panel) and GCMT catalogue (top left-hand panel). The seismological moments are also compared between the body wave and catalogue values of the GCMT and USGS (bottom right-hand panel). Circles are numbered to denote earthquake in date ascending order as listed in Table 1. Note a distributed slip model was not calculated for earthquake 1 (Nyemo County).

normal faulting M5.5+ events compiled by Jackson & White (1989) and Collettini & Sibson (2001) are plotted with those from this study in Fig. 23. These dip estimates are restricted to earthquake solutions which are near pure-normal (rake 270° ± 30°), occurring in the upper continental crust and for which the rupture plane has been determined from surface breaks or from aftershock distributions.

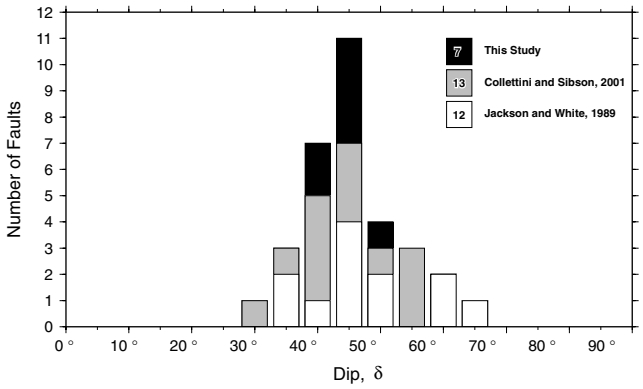

Figure 23. Histogram of active normal fault dip angles from this study (black, seven observations) and from compilations of Jackson & White (1989) and Collettini & Sibson (2001) (white, 12 observations and grey, 13 observations, respectively). The dip data have been assigned to 5° bins, centred on integer multiples of five.

For consistency with previous studies, we have used the body wave seismology fault parameters to provide the estimate for the values of dip and rake. The observations from the InSAR modelling are used to resolve the ambiguity regarding which focal plane represents the slip plane. In the case of the 1992 Damxung earthquake, this was not possible and therefore it was not included in the analysis (although the estimated dip is either 35° or 41°).

None of the seven earthquakes studied here has a low-angle (δ < 30°) fault plane; rather they are tightly clustered in the range 39°–52°, reinforcing the evidence (Jackson & White 1989; Collettini & Sibson 2001) that low-angle fault planes are not found for normal faulting earthquakes whose focal mechanisms can be reliably determined seismologically.

The dips that we measure are at higher angles than those inferred on detachment faults in two of the grabens in southern Tibet. In the Lunggar Rift, south eastern Tibet, Kapp *et al.* (2008) propose detachment faults bounding the fault system, 50–100 km north of the series of three Zhongba earthquakes, which show active normal faulting at 39–46°. However, Kapp *et al.* (2008) indicated that the proposed dips of their detachments were ∼31–33° which, while significantly lower than those observed on the active faults of the region, are still within the range of dips determined from seismology. Similarly in the Yadong Gulu Rift of southeastern Tibet in which the Nyemo and Damxung earthquakes indicate high angle normal faulting (41–52° and 51°, respectively), Kapp *et al.* (2005) propose detachment faults bounding the western edge of the rift,

© 2010 The Authors, *GJI*
Geophysical Journal International © 2010 RAS

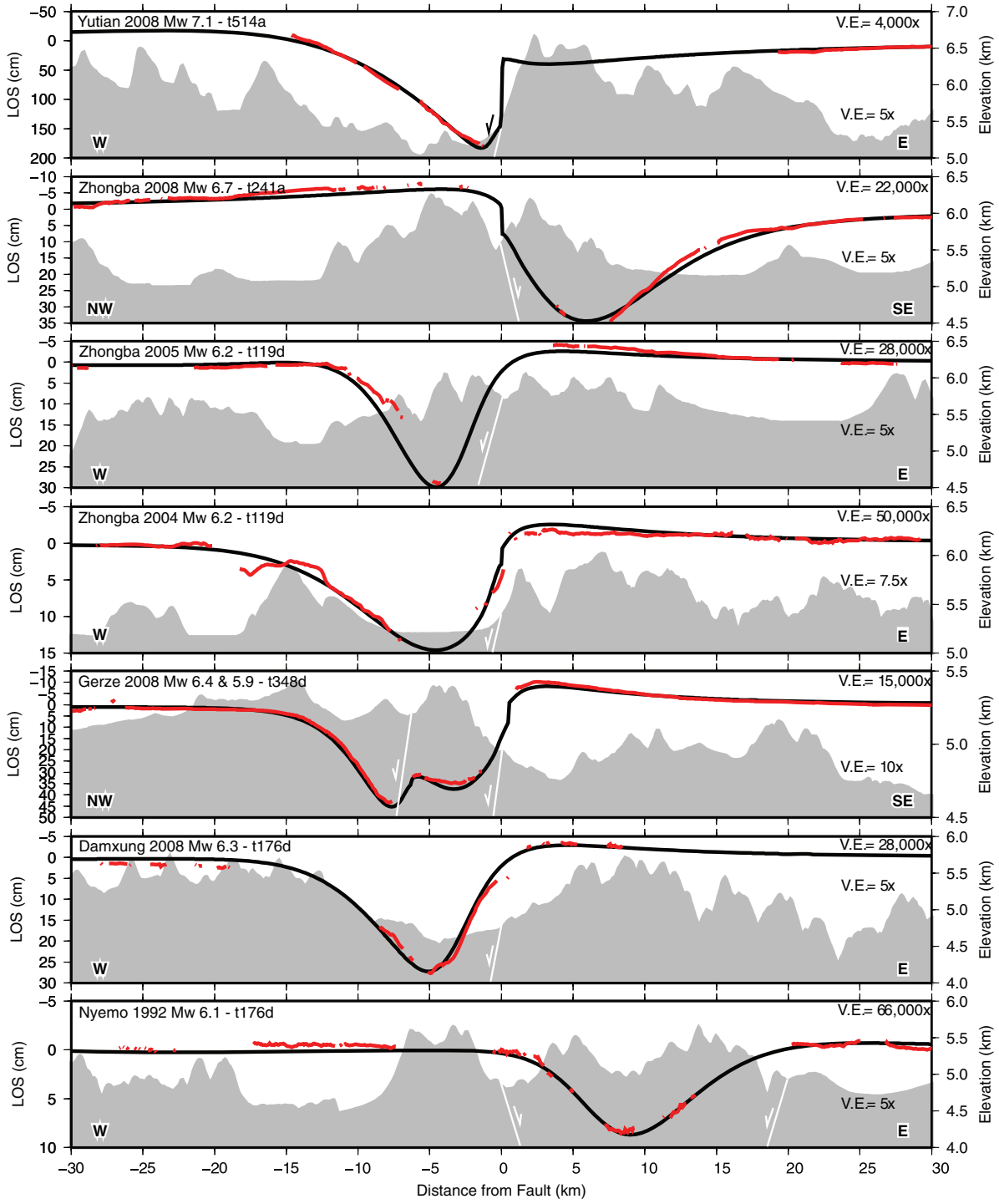

Figure 24. Profiles of line-of-sight deformation and topography taken perpendicular to the faults of the eight earthquakes in this study. Profiles are arranged in geographical order east to west across the plateau. The lines of profiles are shown in Figs 4, 7, 13, 16, A1, A3 and B1. Note the line-of-sight deformation scale is inverted, as positive motion is taken as motion away from the satellite and is largely due to subsidence in the case of these normal faulting events. The interferogram data along the profile is shown in red, the model in black, and the vertical exaggeration is shown in the top right. The topography is shown as grey-scale with the vertical exaggeration shown on the right. Note for the 1992 event, the causative fault is not constrained so the east and west dipping solutions are both shown.

active today with dips in the range 22°–37°, which are significantly lower than the dips of the active faulting measured by InSAR and body wave seismology. One resolution for the discrepancy may be that [as suggested by Kapp *et al.* (2008) for the Lunggar rift], the lower-angle faults are now inactive, and have been rotated to lower dips as a result of slip on the active faults (e.g. Proffett 1977).

7.3.2 Geomorphology of the epicentral areas

Using digital elevation models and Landsat or ASTER satellite imagery, we have looked for any topographic expression associated with the faults on which the eight earthquakes occurred, and also for correlations between the coseismic vertical motions derived

© 2010 The Authors, *GJI*
Geophysical Journal International © 2010 RAS

from the InSAR and topography (Fig. 24). Where this topographic expression has been clear and matches the pattern of InSAR deformation, it has often been an important constraint in our fault models.

The largest event studied, the M_w 7.1 Yutian earthquake, is situated on a clear graben-bounding fault with a relief of over 1 km across the fault (Fig. 10 and 24). Although this fault is not present in the compilation of Taylor & Yin (2009), it was recognised by Armijo *et al.* (1986) in satellite imagery. The next largest event was the 2008 M_w 6.7 Zhongba earthquake which occurred in the Lunggar rift (Fig. 15) on a mapped fault with a clear steep footwall fronted by a low-relief basin. However, the southern fault segment, on which we found larger slip and greater subsidence, actually cuts into the higher topography rather than following the mountain front (Fig. 24). The other two earlier earthquakes that occurred in this area also have variable surface expressions, and are on faults not included in the compilation of Taylor & Yin (2009). The faulting associated with the M_w 6.2 2004 event is clearly seen in the topography, but the M_w 6.2 2005 event has no clear geomorphological expression, with subsidence occurring beneath high topography rather than a basin (Fig. 24).

The pair of Gerze earthquakes (M_w 6.4 and 5.9) both occurred on unmapped faults, immediately north of the left-lateral Riganpei Co Fault (Fig. 6). The main fault has a surface expression in ASTER satellite imagery when examined in detail, but the smaller event has no clear surface trace. Again, the subsidence is located beneath the higher topography rather than the basin floor (Fig. 24). Finally, the M_w 6.3 2008 Damxung and M_w 6.1 1992 Nyemo earthquakes occurred in the Yadong Gulu rift (Fig. 3) and are most likely coincident with mapped faults from Armijo *et al.* (1986). The 2008 earthquake clearly bounds the eastern side of the graben. The 1992 event occurred on the western side of the graben, and the resulting subsidence is beneath high topography, in the footwall of the main mapped fault, an occurrence probably indicative of the relative rates of motion on the two faults.

The association of faulting with topography is therefore varied. The largest earthquakes occurred on known faults (although the southern segment of the 2008 Zhongba event cuts into the high topography rather than following the mapped fault). Others have a clear geomorphic expression but the faults do not appear to have been previously mapped. Although the largest event is clearly related to topography, there otherwise appears to be no simple correlation between earthquake magnitude and geomorphic expression. Hence we conclude that methods of assessing normal faulting on the Tibetan plateau that are based upon current fault compilations or topographically-mapped fault data sets will underestimate the amount of normal faulting, and hence the amount of extension, of the Tibetan plateau.

8 CONCLUSIONS

We conclude from our study of recent normal faulting events in Tibet that significant extension by normal faulting is not restricted to southern Tibet, but occurs widely across the plateau, and we find no evidence for active low-angle normal faulting. Our examination of the relationship between moment release and surface height highlights the strong dependence of extensional faulting on gravitational potential energy. The 2008 M_w 7.1 Yutian earthquake, the largest normal faulting event to have occurred recently on the plateau, took place in the region with the highest average 100-km-scale topography in the world. These observations, and the widespread distribution of faulting, strongly reinforce the theory that the extension of the plateau is driven primarily by gravitational forces.

Whilst the majority of east–west extension probably occurs in M7–8 strike-slip events (Fig. 20), our estimate of east-west strain from summing the last 43 yr of normal faulting earthquakes is 3–4 mm yr^{-1} which accounts for ∼15–20 per cent of the 22 mm yr^{-1} ESE–WNW extension measured by GPS. We observe that, while the larger events are clearly associated with topographic features, significant normal faulting earthquakes occur on faults that have not been mapped or have no clear large-scale surface expression. This suggests that estimates of the total extension from normal faulting based on geomorphology may be underestimated. Large normal faulting earthquakes like those studied here are likely to occur right across the plateau and, when they do occur, to be confined to regions with average surface elevations above 5 km.

ACKNOWLEDGMENTS

This work was supported by the Natural Environmental Research Council (NERC) through the National Centre of Earth Observation (NCEO) of which the Centre for the Observation and Modelling of Earthquakes, Volcanoes and Tectonics (COMET+, http://comet.nerc.ac.uk) is a part, as well as through a studentship to JRE. The InSAR modelling of the 2008 Gerze, 2004 and 2005 Zhongba and the 1992 Nyemo earthquakes formed a part of R. Walters Master's thesis. All ENVISAT SAR data are copyrighted by the European Space Agency and were provided under project AOE-621. All ALOS data are copyrighted by JAXA. We are grateful to JPL/Caltech for use of the ROI_PAC software. Our thanks go to Juliet Biggs, Susanna Ebmeier, Eric Fielding, Mike Floyd, Ed Nissen, David Robinson, Isabelle Ryder, Al Sloan and Tim Wright for help and discussions. Most figures were made using the public domain Generic Mapping Tools (Wessel & Smith 1998).

REFERENCES

Armijo, R., Tapponnier, P., Mercier, J.L. & Tong-Lin, H., 1986. Quaternary extension in southern Tibet: field observations and tectonic implications, *J. geophys. Res.,* **91,** 13 803–13 872.

Armijo, R., Tapponnier, P. & Tonglin, H., 1989. Late Cenozoic right-lateral strike-slip faulting in southern Tibet, *J. geophys. Res.,* **94,** 2787–2838.

Axen, G.J., 2007. Research Focus: Significance of large-displacement, low-angle normal faults, *Geology,* **35,** 287–288.

Bassin, C., Laske, G. & Masters, G., 2000. The current limits of resolution for surface wave tomography in North America, *EOS, Trans. Am. geophys. Un.,* **81,** S12A–03.

Biggs, J., Bergman, E., Emmerson, B., Funning, G.J., Jackson, J., Parsons, B. & Wright, T.J., 2006. Fault identification for buried strike-slip earthquakes using InSAR: the 1994 and 2004 Al Hoceima, Morocco earthquakes, *Geophys. J. Int.,* **166,** 1347–1362.

Cattin, R. & Avouac, J.P., 2000. Modeling mountain building and the seismic cycle in the Himalaya of Nepal, *J. geophys. Res.,* **105,** 13 389–13 408.

Collettini, C. & Sibson, R.H., 2001. Normal faults, normal friction?, *Geology,* **29,** 927–930.

Du, Y., Aydin, A. & Segall, P., 1992. Comparison of various inversion techniques as applied to the determination of a geophysical deformation model for the 1983 Borah Peak earthquake., *Bull. seism. Soc. Am.,* **82,** 1840–1866.

Dziewonski, A.M. & Woodhouse, J.H., 1983. An experiment in systematic study of global seismicity Centroid-moment tensor solutions for 201 moderate and large earthquakes of 1981, *J. geophys. Res.,* **88,** 3247–3271.

Dziewonski, A.M., Chou, T.A. & Woodhouse, J.H., 1981. Determination of earthquake source parameters from waveform data for studies of global and regional seismicity, *J. geophys. Res.,* **86,** 2825–2852.

© 2010 The Authors, *GJI*
Geophysical Journal International © 2010 RAS

Ekström, G., Dziewoński, A.M., Maternovskaya, N.N. & Nettles, M., 2005. Global seismicity of 2003: centroid moment-tensor solutions for 1087 earthquakes, *Phys. Earth planet. Inter.,* **148,** 327–351.

Elliott, J.R., Biggs, J., Parsons, B. & Wright, T.J., 2008. InSAR slip rate determination on the Altyn Tagh Fault, northern Tibet, in the presence of topographically correlated atmospheric delays, *Geophys. Res. Lett.,* **35,** L12309, doi:10.1029/2008GL033659.

Engdahl, E.R., van der Hilst, R. & Buland, R., 1998. Global teleseismic earthquake relocation with improved travel times and procedures for depth determination, *Bull. seism. Soc. Am.,* **88**(3), 722–743.

England, P.C. & Houseman, G.A., 1989. Extension during continental convergence, with application to the Tibetan Plateau, *J. geophys. Res.,* **94,** 17 561–17 579.

Farr, T. & Kobrick, M., 2000. Shuttle radar topography mission produces a wealth of data, *EOS, Trans. Am. geophys. Un.,* **81,** 583–585.

Feigl, K.L., Sergent, A. & Jacq, D., 1995. Estimation of an earthquake focal mechanism from a satellite radar interferogram: application to the December 4, 1992 Landers aftershock, *Geophys. Res. Lett.,* **22,** 1037–1040.

Funning, G.J., Parsons, B., Wright, T.J., Jackson, J.A. & Fielding, E.J., 2005. Surface displacements and source parameters of the 2003 Bam (Iran) earthquake from Envisat advanced synthetic aperture radar imagery, *J. geophys. Res.,* **110**(B9), B09406, doi:10.1029/2004JB003338.

Funning, G.J., Parsons, B. & Wright, T.J., 2007. Fault slip in the 1997 Manyi, Tibet earthquake from linear elastic modelling of InSAR displacements, *Geophys. J. Int.,* **169,** 988–1008.

Goldstein, R.M. & Werner, C.L., 1998. Radar interferogram filtering for geophysical applications, *Geophys. Res. Lett.,* **25,** 4035–4038.

Goldstein, R.M., Zebker, H.A. & Werner, C.L., 1988. Satellite radar interferometry—two-dimensional phase unwrapping, *Radio Sci.,* **23,** 713–720.

Hanssen, R.F., 2001. *Radar Interferometry: Data Interpretation and Analysis,* Kluwer Acad., Norwell, MA.

Houseman, G. & England, P., 1986. Finite strain calculations of continental deformation. I—method and general results for convergent zones. II—comparison with the India-Asia collision zone, *J. geophys. Res.,* **91,** 3651–3676.

Jackson, J.A. & White, N.J., 1989. Normal faulting in the upper continental crust: observations from regions of active extension, *J. Struct. Geol.* **11,** 15–36.

Jonsson, S., Zebker, H., Segall, P. & Amelung, F., 2002. Fault slip distribution of the M_w 7.2 Hector Mine earthquake estimated from satellite radar and GPS measurements., *Bull. seism. Soc. Am.,* **92,** 1377–1389.

Kapp, J.L.D., Harrison, T.M., Kapp, P., Grove, M., Lovera, O.M. & Lin, D., 2005. Nyainqentanglha Shan: a window into the tectonic, thermal, and geochemical evolution of the Lhasa block, southern Tibet, *J. geophys. Res.,* **110,** B08413, doi:10.1029/2004JB003330.

Kapp, P., Taylor, M., Stockli, D. & Ding, L., 2008. Development of active low-angle normal fault systems during orogenic collapse: insight from Tibet, *Geology,* **36**(1), 7–10.

Kostrov, V.V., 1974. Seismic moment and energy of earthquakes and seismic flow of rock, *Izv. Acad. Sci. USSR Phys. Earth Physics,* **1,** 23–40.

Lasserre, C., Peltzer, G., Crampé, F., Klinger, Y., Van der Woerd, J. & Tapponnier, P., 2005. Coseismic deformation of the 2001 $M_{\rm w}$ = 7.8 Kokoxili earthquake in Tibet, measured by synthetic aperture radar interferometry, *J. geophys. Res.,* **110,** B12408, doi:10.1029/2004JB003500.

Lohman, R.B. & Simons, M., 2005. Some thoughts on the use of InSAR data to constrain models of surface deformation: noise structure and data downsampling, *Geochem. Geophys. Geosyst.,* **6,** Q01007, doi:10.1029/2004GC000841.

McCaffrey, R. & Abers, G., 1988. SYN3: A program for inversion of teleseismic body waveforms on microcomputers, Air Force Geophysics Laboratory Technical Report AFGL-TR-0099, Hanscomb Air Force Base, Massachusetts.

Molnar, P. & Chen, W.-P., 1983. Focal depths and fault plane solutions of earthquakes under the Tibetan plateau, *J. geophys. Res.,* **88,** 1180–1196.

Molnar, P. & Lyon-Caen, H., 1989. Fault plane solutions of earthquakes and active tectonics of the Tibetan Plateau and its margins, *Geophys. J. Int.,* **99,** 123–154.

Molnar, P. & Qidong, D., 1984. Faulting associated with large earthquakes and the average rate of deformation in central and eastern Asia, *J. geophys. Res.,* **89,** 6203–6228.

Molnar, P. & Tapponnier, P., 1978. Active tectonics of Tibet, *J. geophys. Res.,* **83,** 5361–5376.

Molnar, P., England, P. & Martinod, J., 1993. Mantle dynamics, uplift of the Tibetan Plateau, and the Indian monsoon, *Rev. Geophys.,* **31,** 357–396.

Okada, Y., 1985. Surface deformation due to shear and tensile faults in a half-space, *Bull. seism. Soc. Am.,* **75**(4), 1135–1154.

Press, W.H., Teukolsky, S.A., Vetterling, W.T. & Flannery, B.P., 1992. *Numerical Recipes in C: The Art of Scientific Computing,* 2nd edn, Cambridge University Press, Cambridge.

Proffett, J.M., 1977. Cenozoic geology of the Yerington district, Nevada, and implications for the nature and origin of Basin and Range faulting, *Geol. Soc. Am. Bull.,* **88,** 247–266.

Raterman, N.S., Cowgill, E. & Lin, D., 2007. Variable structural style along the Karakoram fault explained using triple-junction analysis of intersecting faults, *Geosphere,* **3,** 71–85.

Rosen, P.A., Hensley, S., Peltzer, G. & Simons, M., 2004. Updated repeat orbit interferometry package released, *EOS, Trans. Am. geophys. Un.,* **85,** 47–47.

Scholz, C.H., 2002. *The Mechanics of Earthquakes and Faulting,* Cambridge University Press, Cambridge.

Scholz, C.H. & Cowie, P.A., 1990. Determination of total strain from faulting using slip measurements, *Nature,* **346,** 837–839.

Steck, L.K., Phillips, W.S., Mackey, K., Begnaud, M.L., Stead, R.J. & Rowe, C.A., 2009. Seismic tomography of crustal *P* and *S* across Eurasia, *Geophys. J. Int.,* **177,** 81–92.

Sun, J., Shen, Z., Xu, X. & Bürgmann, R., 2008. Synthetic normal faulting of the 9 January 2008 Nima (Tibet) earthquake from conventional and along-track SAR interferometry, *Geophys. Res. Lett.,* **35,** L22308, doi:10.1029/2008GL035691.

Taylor, M. & Yin, A., 2009. Active structures of the Himalayan-Tibetan orogen and their relationships to earthquake distribution, contemporary strain field, and Cenozoic volcanism, *Geosphere,* **5**(3), 199–214.

Taylor, M., Yin, A., Ryerson, F.J., Kapp, P. & Ding, L., 2003. Conjugate strike-slip faulting along the Bangong-Nujiang suture zone accommodates coeval east-west extension and north-south shortening in the interior of the Tibetan Plateau, *Tectonics,* **22**(4), 18, doi:10.1029/2002TC001361.

Wessel, P. & Smith, W.H.F., 1998. New, improved version of generic mapping tools released, *EOS, Trans. Am. geophys. Un.,* **79,** 579–579.

Wright, T.J., Parsons, B.E., Jackson, J.A., Haynes, M., Fielding, E.J., England, P.C. & Clarke, P.J., 1999. Source parameters of the 1 October 1995 Dinar (Turkey) earthquake from SAR interferometry and seismic bodywave modelling, *Earth planet. Sci. Lett.,* **172,** 23–37.

Wright, T.J., Lu, Z. & Wicks, C., 2003. Source model for the M_w 6.7, 23 October 2002, Nenana Mountain Earthquake (Alaska) from InSAR, *Geophys. Res. Lett.,* **30,** SDE12, doi:10.1029/2003GL018014.

Wright, T.J., Lu, Z. & Wicks, C., 2004. Constraining the Slip Distribution and Fault Geometry of the Mw 7.9, 3 November 2002, Denali Fault earthquake with interferometric synthetic aperture radar and global positioning system data, *Bull. seism. Soc. Am.,* **94**(6B), S175–189.

Wright, T.J., Parsons, B., England, P.C. & Fielding, E.J., 2004. InSAR observations of low slip rates on the major faults of Western Tibet, *Science,* **305,** 236–239.

Yin, A. *et al.*, 1999. Significant late Neogene east-west extension in northern Tibet, *Geology,* **27,** 787–791.

Zhang, P.-Z. *et al.*, 2004. Continuous deformation of the Tibetan Plateau from global positioning system data, *Geology,* **32,** 809–812.

Zwick, P., McCaffrey, R. & Abers, G., 1994. MT5 Program, *IASPEI Software Library,* **4**.

© 2010 The Authors, *GJI*
Geophysical Journal International © 2010 RAS

APPENDIX A: ZHONGBA COUNTY 2004 AND 2005 EARTHQUAKES

Two relatively recent and moderately sized normal faulting events preceded the 2008 earthquake in Zhongba county. A westward dipping fault ruptured on 2004 July 11, 30 km ESE of the 2008 event and a similar earthquake occurred nine months later, a further 20 km south on 2005 April 7 (Fig. 15).

IS2 ascending and descending ENVISAT acquisition pairs are available covering the 2004 event (Table A1), but the acquisition interval of the ascending pair spans both the 2004 and 2005 earthquakes. The deformation signals from the two events are largely

Table A1. Details of interferograms for the Zhongba County M_w 6.2 earthquake 2004 July 11 (23:09 UTC) and M_w 6.2 earthquake 2005 April 7 (20:05 UTC). Caption as for Table 2.

Satellite	Track no.	Inclination (asc/dsc)	Angle (°)	Master (yy/mm/dd)	Slave (yy/mm/dd)	ΔT (dys)	ΔPT (dys)	$B_\perp$ (m)	Data (pts)	Weight	RMS (cm)		
											Uniform	Fix λ	Vary λ
					2004 July 11 earthquake								
Env	119	dsc	23	040317	040908	175	59	70	705	1	0.7	0.6	0.6
Env	384	asc	23	040229	050529	455	322	145	597	1	1.1	0.8	0.8
					2005 April 7 earthquake								
Env	119	dsc	23	050302	050615	105	69	52	1428	1	1.5	1.5	1.3
Env	384	asc	23	041031	050703	245	87	128	1429	1	1.4	0.9	0.9
Env	470	asc	41	041002	050813	315	128	470	716	1	2.6	1.9	1.6

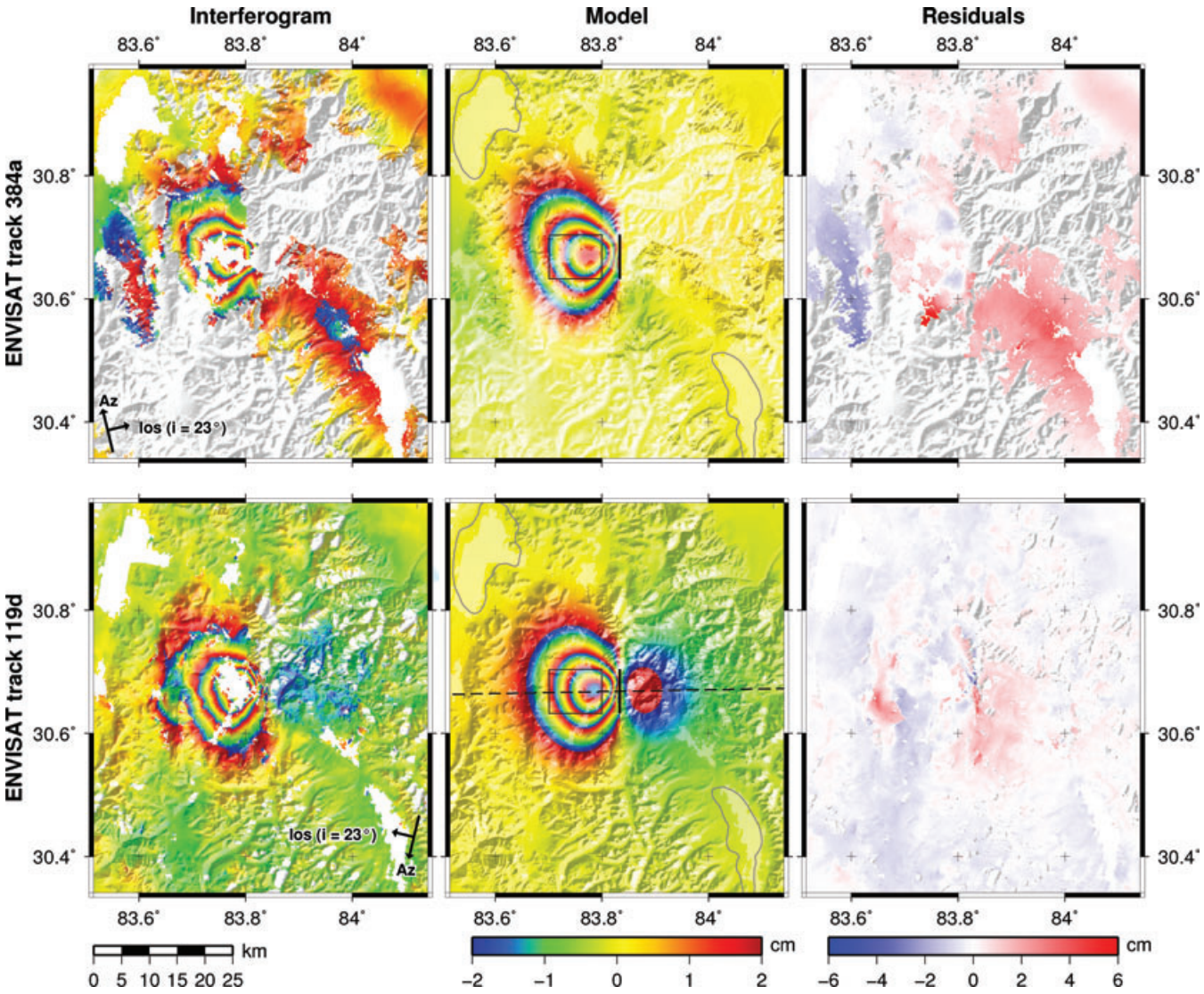

Figure A1. The Zhongba 2004 earthquake interferograms for distributed slip modelling with fixed rake. Details as for Fig. 4.

© 2010 The Authors, *GJI*
Geophysical Journal International © 2010 RAS

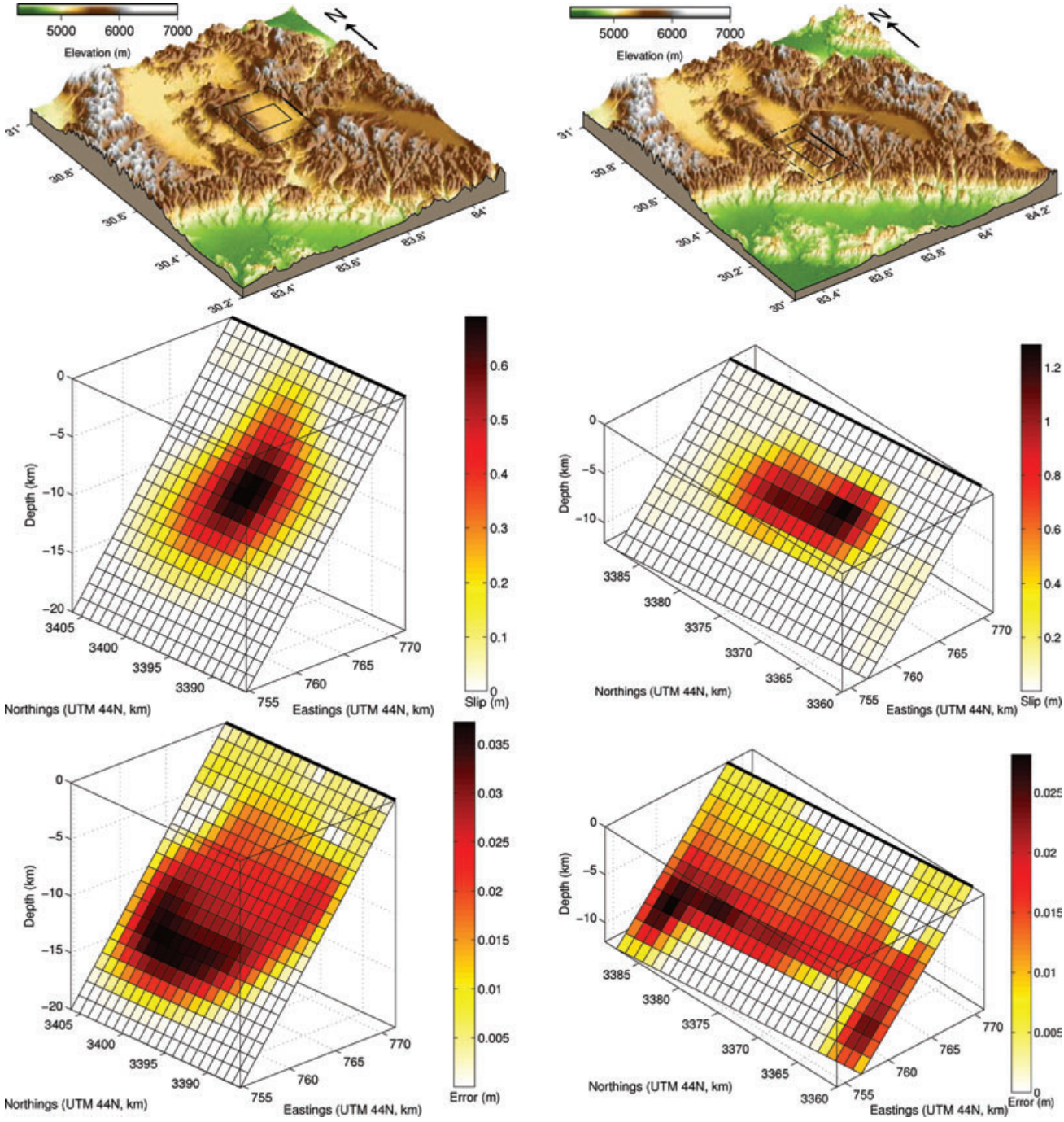

Figure A2. Left-hand panel: Zhongba 2004 earthquake slip distribution with fixed rake based upon the fault orientation from uniform slip modelling. Right-hand panel: Zhongba 2005 earthquake slip distribution with fixed rake based upon the fault orientation from uniform slip modelling. Caption as for Fig. 9.

spatially separate in the ascending interferogram, with a small area of significant interference at the southern edge of the 2004 deformation signal. Therefore, after a model was obtained for the 2005 earthquake, the forward model of this earthquake was subtracted from the ascending interferogram prior to down-sampling. In all other respects, the data were processed, down-sampled, and modelled as described in the main text.

For the 2004 earthquake, the maximum line-of-sight deformation for both ascending and descending interferograms is ∼15 cm away from the satellite and the deformation signals are qualitatively consistent with normal slip on a west-dipping fault plane (Fig. A1). With no parameters fixed during the inversion process, the inversion for uniform slip converges on a west-dipping solution. The surface projection of the model fault runs parallel to a mountain range-front that is most likely tectonically generated by this fault, but is located in an area of high topography. We therefore offset the fault and fix its location to the sharp break in slope at the front of the range, and invert again for all other parameters. This inversion again converges easily to a similar solution.

© 2010 The Authors, *GJI*
Geophysical Journal International © 2010 RAS

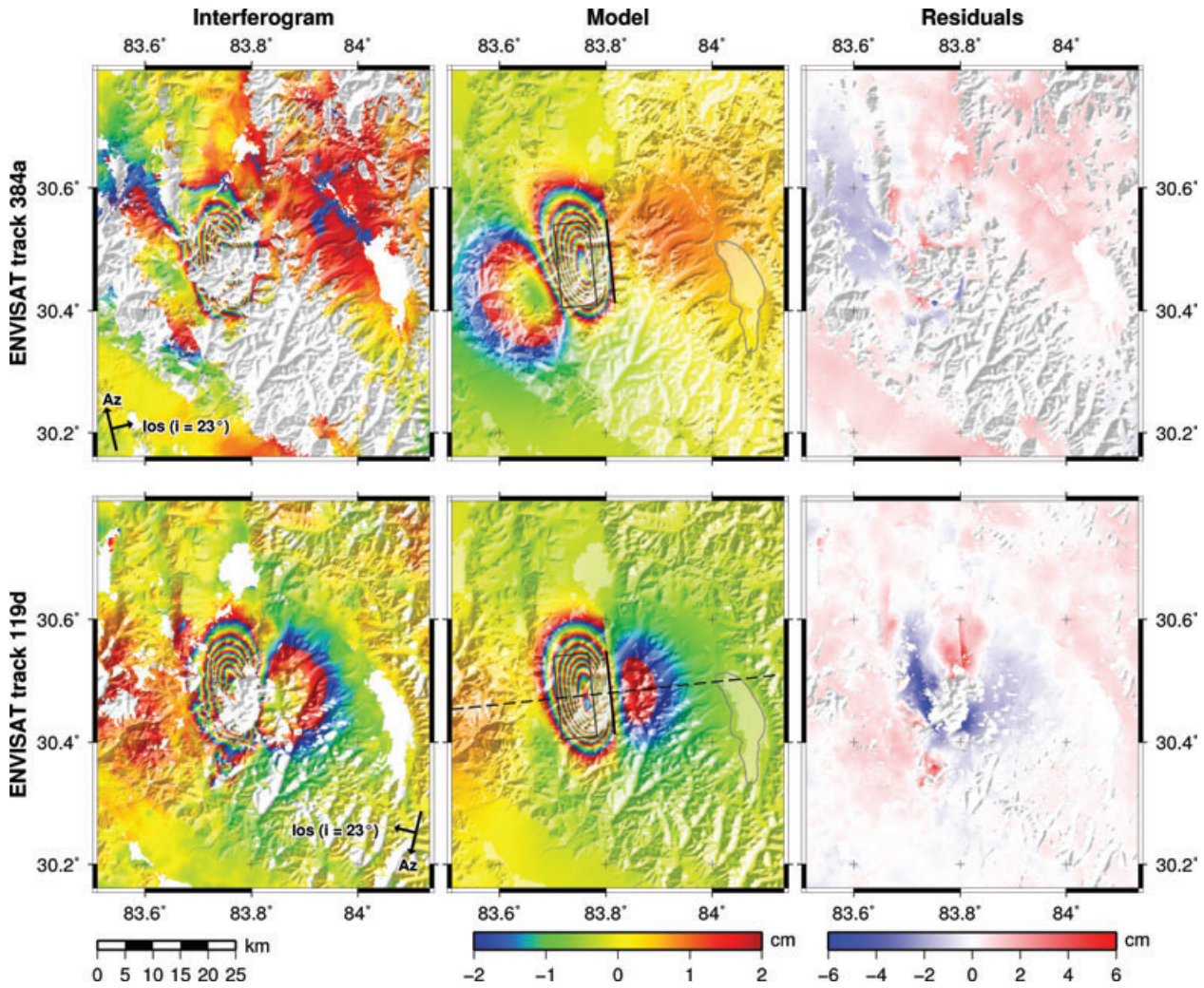

Figure A3. Zhongba 2005 earthquake interferograms for distributed slip modelling with fixed rake. The interferogram for the other track used in the modelling but not shown here is given in the on-line supporting information. Details as for Fig. 4.

This best-fitting solution describes a fault with short length but large downdip width. These fault plane extents are physically unrealistic but probably represent the best approximation for a uniform-slip model. This model is therefore only used to fix the fault geometry during the variable slip inversion, and does not represent a viable model in its own right. From Landsat imagery it is clear that the surface trace for the model fault runs sub parallel to a large mountain range front, and the strike of this trace corresponds closely to a linear offset feature in alluvial fans running off the range front. The data were also inverted for a fault with strike constrained to reflect an east-dipping fault but the inversion did not converge easily on a solution, and the solution had a larger rms than for the best-fitting west-dipping model. Therefore only the west-dipping uniform model is presented here (Table A2), and is used as the basis for the distributed-slip model. Distributed slip modelling improves the fit to the data and produces more realistic fault-plane extents (Figs A1 and A2).

For the Zhongba 2005 earthquake, three ENVISAT acquisition pairs were available with independent viewing geometries: IS2 ascending, IS6 ascending, and IS2 descending. Interferograms were processed as described in the main text. Deformation signals show maximum line-of-sight deformation of 30, 40 and 29 cm for the IS2 ascending, IS6 ascending, and IS2 descending interferograms respectively (Fig. A3). A large proportion of the IS6 ascending interferogram shows decorrelation and so this data set was down-sampled to half the number of data points that were sampled from each of the two IS2 interferograms. Each down-sampled data set was then weighted equally during inversion. The uniform slip inversion process failed to converge easily on a solution and so slip was fixed at 0.7 m using the method described in the main text. The best-fitting solution from uniform slip modelling describes a west-dipping rectangular fault plane with a large length but small downdip extent. This fault plane geometry is used to solve for distributed slip along the fault to produce the model shown in Figs A2 and A3. The surface trace of the model fault for the 2005 earthquake is not associated with any clear active tectonic features, instead running through a glacial valley.

We attempted to model the fault with an eastward dipping plane, but the asymmetry seen in the fringe spacing of the data interferograms was not reproduced in the model, nor the sharp turn in the fringes observed in the lower right-hand corner of the main deformation lobe (Fig. A3), resulting in a worse rms misfit when compared to that for the westward dipping fault solution. Furthermore, the

© 2010 The Authors, *GJI*
Geophysical Journal International © 2010 RAS

Table A2. 2004-05 Zhongba County fault plane parameters from inverting interferometric data, from *P* and *SH* body wave modelling, and as listed in the GCMT and USGS catalogues. Details as for Table 3 with hypocentral locations from the ISC and EHB catalogues.

Model	Strike (°)	Dip (°)	Rake (°)	Slip (m)	Longitude (°)	Latitude (°)	Length (km)	Top (km)	Bottom (km)	Centroid (km)	Moment, $M_0 \times 10^{18}$ (Nm)	M_w
2004 July 11 earthquake												
InSAR-u	180	50	282	0.6	83.83	30.67	7.9	3.8	15.1	9.5	2.2	6.2
	±2	±1	±3	±0.1	fixed	fixed	±0.4	±0.2	±0.4	±0.2	±0.06	
InSAR-d-fr	180	50	282	0.3	83.83	30.67	17	1	16	9	2.3	6.2
InSAR-d-vr	180	50	288	0.3	83.83	30.67	19	1	17	9	2.4	6.2
Body wave	159	39	270				11	5	13	9	2.4	6.2
GCMT	156	47	254		83.78	30.56				13	2.4	6.2
USGS	162	45	257		83.67	30.69				8	2.2	6.2
ISC					83.66	30.72				8		6.2*
EHB					83.65	30.68				13		
2005 April 7 earthquake												
InSAR-u	174	40	292	0.7	83.81	30.48	15.1	2.7	8	5	2.8	6.2
	±1	±1	±1	fixed	±0.05 km	±0.06 km	±0.1	±0.1	±0.1	±0.1	±0.03	
InSAR-d-fr	174	40	292	0.5	83.81	30.48	20	2	9	5.5	3.2	6.2
InSAR-d-vr	174	40	297	0.4	83.81	30.48	28	2	11	6.5	4.0	6.3
Body wave	169	40	277				11	1	9	5	2.7	6.2
GCMT	171	43	270		83.72	30.23				12	3.0	6.2
USGS	175	44	264		83.68	30.46				6	2.4	6.2
ISC					83.66	30.52				15		6.1*
EHB					83.66	30.48				8		

*M_s

eastward dip angle disagreed by 15° with our seismological solution, whereas that for the westward exactly matched.

For both the Zhongba 2004 and 2005 earthquakes, fault parameters from InSAR and body wave modelling are compared with seismic catalogue solutions in Table A2. Monte Carlo analysis shows that InSAR model fault parameters for both faults are well resolved. All fault parameters show small 1σ errors, but this is partly a result of fixing parameters during the inversion process.

APPENDIX B: NYEMO COUNTY 1992 EARTHQUAKE

Prior to the Damxung county earthquake in 2008, a M_w 6.1 event on the 1992 July 30 (08:25 UTC) occurred 20 km WSW on a similar N–S striking normal fault (Fig. 3). Only a single descending look direction is available and the pair of suitable ERS-1 acquisitions is shown in Table B1.

Maximum line-of-sight deformation for the interferogram is ∼8 cm away from the satellite (Fig. B1) and the single lobe of subsidence is consistent with normal faulting along a ∼N–S fault. The absence of a footwall uplift signal means that we cannot easily distinguish between west-dipping and east-dipping fault models. Therefore we run two inversions with starting parameters set to the two nodal planes of our body wave solution (Table B2). For all uniform slip inversions, the inversions fail to converge on a solution with reasonable slip, and so slip is fixed to 0.5 m using the method outlined previously. Fault parameters from InSAR and body wave solutions for both possible fault planes for the 1992 Nyemo county earthquake are compared with seismic catalogue solutions in Table B2.

The rms misfits between the InSAR data and model for the two dip directions are indistinguishable (0.45 cm for the eastward dipping compared with 0.47 cm for the west). However, the east-dipping solution matches our body wave strike and dip much better than the west-dipping plane (Table B2). As such, we prefer the east-dipping solution (Fig. B1). The surface projections of either east or west dipping model faults are not associated with any clear surface features.

Monte Carlo analysis shows that InSAR model fault parameters for both possible models are fairly poorly resolved with large 1σ errors for strike, dip and rake (5–15°) and location (1–3 km). These large uncertainties are likely to be due to the deep focus and resulting small surface deformation for this earthquake, making the inversion of the data sensitive to relatively small perturbations with noise. In addition, the lack of ascending track data for this earthquake means that the model is less well constrained than if multiple look directions were available.

Table B1. Details of interferograms for the Nyemo County M_w 6.1 earthquake 1992 July 30 (08:25 UTC). Caption as for Table 2.

Satellite	Track no.	Inclination (asc/dsc)	Incidence (°)	Master (yymmdd)	Slave (yymmdd)	ΔT ΔT (dys)	ΔPT (dys)	$B_\perp$ (m)	Data (pts)	RMS (cm)	
										East	West
ERS-1	176	dsc	23	920618	921210	175	133	76	1525	0.45	0.47

© 2010 The Authors, *GJI*
Geophysical Journal International © 2010 RAS

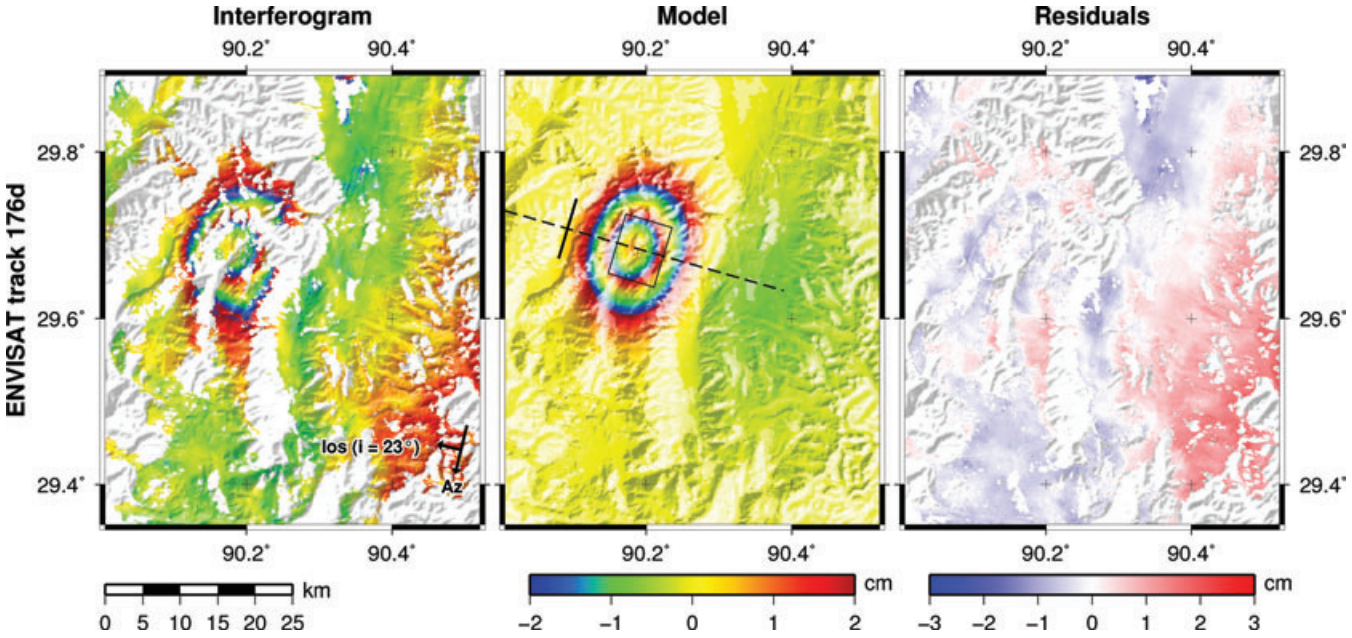

Figure B1. Nyemo 1992 earthquake interferograms for uniform slip modelling assuming a eastward dipping fault plane. Details as for Fig. 4.

Table B2. Nyemo County 1992 fault plane parameters from inverting interferometric data, from *P* and *SH* body wave modelling, and as listed in the GCMT and USGS catalogues. Caption as for Table 3 with hypocentral locations from the ISC and EHB catalogues.

Model	Strike (°)	Dip (°)	Rake (°)	Slip (m)	Longitude (°)	Latitude (°)	Length (km)	Top (km)	Bottom (km)	Centroid (km)	Moment, $M_0 \times 10^{18}$ (Nm)	M_w
InSAR-u	198	35	275	0.5	90.28	29.65	9.1	6.5	10.5	8.5	1.0	5.9
West	±8	±5	±10	fixed	±1.4 km	±1.9 km	±1.1	±0.3	±0.7	±0.4	±0.1	
InSAR-u	017	41	270	0.5	90.09	29.70	8.3	6.1	11.7	8.9	1.1	6.0
East	±15	±5	±12	fixed	±1.2 km	±3.0 km	±1.2	±0.4	±0.7	±0.4	±0.1	
Body wave	175/024	52/41	251/293				9	7	13	10	1.0	5.9
GCMT	196/010	49/42	274/266		90.30	29.46				15	1.8	6.1
USGS	251/107	48/48	244/296		90.16	29.58				10	1.7	6.1
ISC					90.18	29.57				31		6.0*
EHB					90.20	29.58				14		

*M_s

SUPPORTING INFORMATION

Additional Supporting Information may be found in the online version of this article:

Appendices C–F. This file contains the online-only appendices. Appendix C contains the seismological body wave solutions for each event. Appendix D includes the interferogram figures used in the fault modelling of the Yutian and Zhongba 2008/2005 earthquakes that are not present in the main body of the paper. Appendix E contains the SAR time coverage for each of the eight events. Appendix F presents tables of slip distributions for the Yutian, all three Zhongba and both the Gerze earthquakes from the InSAR distributed slip modelling.

Please note: Wiley-Blackwell are not responsible for the content or functionality of any supporting materials supplied by the authors. Any queries (other than missing material) should be directed to the corresponding author for the article.

© 2010 The Authors, *GJI*
Geophysical Journal International © 2010 RAS